The Cryosphere Discuss., 8, 2867–2922, 2014
www.the-cryosphere-discuss.net/8/2867/2014/
doi:10.5194/tcd-8-2867-2014

The Cryosphere Discussions
Open Access

Processes governing the mass balance of Chhota Shigri Glacier (Western Himalaya, India) assessed by point-scale surface energy balance measurements

M. F. Azam[1,2], **P. Wagnon**[1,3], **C. Vincent**[4], **AL. Ramanathan**[2], **A. Mandal**[2], **and J. G. Pottakkal**[2]

[1]IRD/UJF – Grenoble I/CNRS/G-INP, LGGE UMR 5183, LTHE UMR 5564, 38402 Grenoble Cedex, France
[2]School of Environmental Sciences, Jawaharlal Nehru University, New Delhi 110067, India
[3]ICIMOD, GP.O. Box 3226, Kathmandu, Nepal
[4]UJF – Grenoble I/CNRS, LGGE UMR 5183, 38041 Grenoble Cedex, France

Received: 26 April 2014 – Accepted: 20 May 2014 – Published: 5 June 2014

Correspondence to: M. F. Azam (farooqaman@yahoo.co.in, farooq.azam@lgge.obs.ujf-grenoble.fr)

Published by Copernicus Publications on behalf of the European Geosciences Union.

Abstract

Recent studies revealed that Himalayan glaciers have been shrinking at an accelerated rate since the beginning of the 21st century. However the climatic causes for this shrinkage remain unclear given that surface energy balance studies are almost nonexistent in this region. In this study, a point-scale surface energy balance analysis was performed using in-situ meteorological data from the ablation zone of Chhota Shigri Glacier over two separate periods (August 2012 to February 2013 and July to October 2013) in order to understand the response of mass balance to climate change. Energy balance numerical modeling provides quantification of the surface energy fluxes and identification of the factors affecting glacier mass balance. The computed ablation was validated by stake observations. During summer-monsoon period, net radiation was the primary component of the surface energy balance with 82 % of the total heat flux which was complimented with turbulent sensible and latent heat fluxes with a share of 13 % and 5 %, respectively. A striking feature of energy balance is the positive turbulent latent heat flux, thus condensation or re-sublimation of moist air at the glacier surface takes place, during summer-monsoon period which is characterized by relatively high air temperature, high relative humidity and almost permanent melting surface. The impact of Indian summer monsoon on Chhota Shigri Glacier mass balance has also been assessed. This analysis demonstrates that the intensity of snowfall events during the summer-monsoon season plays a key role on surface albedo, in turn on melting, and thus is among the most important drivers controlling the annual mass balance of the glacier. Summer-monsoon air temperature, controlling the precipitation phase (rain vs. snow and thus albedo), counts, indirectly, also among the most important drivers for the glacier mass balance.

TCD
8, 2867–2922, 2014

1 Introduction

Himalayan glaciers, located on Earth's highest mountain range, provide the sources to numerous rivers that supply water to millions of people in Asia (e.g., Kaser et al., 2010; Immerzeel et al., 2013). Some recent studies have found negative mass balances over Himalayan glaciers (e.g., Azam et al., 2012; Bolch et al., 2012; Kääb et al., 2012; Gardelle et al., 2013), with the fact that the Himalayan glaciers (22 800 km^2) have been shrinking at an accelerated rate since the beginning of 21st century (Bolch et al., 2012; Azam et al., 2014). Glacial retreat and significant mass loss may not only cause natural hazards such as landslides and glacier lake outburst floods but also endanger water resources in long term (Thayyen and Gergan, 2010; Immerzeel et al., 2013).

Unfortunately, data on recent glacier changes are sparse and even sparser as we go back in time (Cogley, 2011; Bolch et al., 2012) and, thus, the rate at which these glaciers are changing remains poorly constrained (Vincent et al., 2013). The erroneous statement in the Intergovernmental Panel on Climate Change (IPCC) Fourth Assessment Report (IPCC, 2007) about the future of Himalayan glacier has highlighted our poor understanding of the behavior of the region's glaciers to climate. However, the IPCC Fifth Assessment Report (IPCC, 2013) stated "Several studies of recent glacier velocity change (Azam et al., 2012; Heid and Kääb, 2012) and of the worldwide present-day sizes of accumulation areas (Bahr et al., 2009) indicate that the world's glaciers are out of balance with the present climate and thus committed to losing considerable mass in the future, even without further changes in climate". A reliable prediction of the responses of Himalayan glaciers towards future climatic change and their potential impacts on the regional population requires the present understanding of the physical relationship between these glaciers and climate. This relationship can be addressed in details by studying glacier surface energy balance (hereafter SEB).

Comprehensive glacier SEB studies were started in the early 1950s (e.g., Hoinkes, 1953) and since then our understanding of glacier–climate relationship have been improving. SEB studies, of the world's glaciers and ice sheets, have been conducted ex-

TCD
8, 2867–2922, 2014

tensively in the Alps (e.g., Klok and Oerlemans, 2002; Oerlemans and Klok, 2002), in Antarctica (e.g., Favier et al., 2011; Kuipers Munneke et al., 2012), in Greenland (e.g., Van den Broeke et al., 2011), in the tropics (e.g., Wagnon et al., 1999, 2001, 2003; Favier et al., 2004; Sicart et al., 2005, 2011; Nicholson et al., 2013), but not yet in High Asia Mountains. However, on these mountains, a few studies have been carried out mainly in Tian Shan (Li et al., 2011), in Qilian mountains (Sun et al., 2014), in Tibetan Plateau (Yang et al., 2011; Mölg et al., 2012; Zhang et al., 2013) and in the Nepalese Himalaya (Kayastha et al., 1999; Lejeune et al., 2013). Unfortunately glacier SEB studies from Indian Himalaya (covering Western, some Central and Eastern parts of Himalaya) are not available. Therefore, there is an urgent need to conduct detailed SEB studies in different regions of Himalaya. In fact, SEB studies are of crucial importance because glaciers across the Himalayan range have different mass balance behaviors (Gardelle et al., 2013), depending on their different climatic setup. For example, glaciers in Nepal receive almost all their annual precipitation from the Indian summer monsoon (ISM), thus these are summer-accumulation type glaciers (Ageta and Higuchi, 1984; Wagnon et al., 2013). Besides, Chhota Shigri and other glaciers in Western Himalaya receive precipitation both from the ISM in summer and from mid-latitude westerlies (MLW) in winter (Shekhar et al., 2010).

Chhota Shigri Glacier is one of the best studied glaciers in Indian Himalaya. Between 2002 and 2013, annual field measurements revealed that the glacier lost mass at a rate of -0.59 ± 0.40 m w.e. a^{-1} (Ramanathan, 2011; Azam et al., 2014). The volume change of Chhota Shigri Glacier has also been measured between 1988 and 2010 using in-situ geodetic measurements by Vincent et al. (2013), revealing a moderate mass loss over this 2 decade-period (-3.8 ± 2.0 m w.e. corresponding to -0.17 ± 0.09 m w.e. a^{-1}). Combining the latter result with field measurements and digital elevation models differencing from satellite images, they deduced a slightly positive or near-zero mass balance between 1988 and 1999 ($+1.0 \pm 2.7$ m w.e. corresponding to $+0.09 \pm 0.24$ m w.e. a^{-1}). Further, Azam et al. (2014) reconstructed the annual mass balances of Chhota Shigri Glacier between 1969 and 2012 using a degree-day approach and an accumulation

TCD
8, 2867–2922, 2014

model fed by long-term meteorological data recorded at Bhuntar meteorological station (~ 50 km south of the glacier, 1092 m a.s.l.) and discussed the mass balance pattern at decadal level. They also compared the decadal mass balances with meteorological variables and suggested that winter precipitation and summer temperature are almost equally important drivers controlling the mass balance pattern of this glacier. A period of steady state between 1986 and 2000 and an accelerated mass wastage after 2000 were also defined.

Present studies on the climate sensitivity of Western/Indian Himalayan glaciers either come from empirical analysis at decadal level (Azam et al., 2014) or based on basic comparison between meteorological variables and glacier mass balance (Koul and Ganjoo, 2010), emphasizing the lack of physical understanding of the glacier–climate relationship in this region. Therefore, a detailed analysis of the SEB yet remains underway for Western/Indian Himalayan glaciers. Use of Automatic weather station (AWS) provides the noble opportunity to obtain long and continuous records of meteorological data and to study the seasonal and inter-annual variations in SEB at point locations (e.g., Oerlemans, 2000; Reijmer and Oerlemans, 2002; Mölg and Hardy, 2004). The present study is focused on the SEB analysis of Chhota Shigri Glacier, using in-situ AWS measurements. It involves two main objectives: (1) the glacier's microclimate is analyzed, (2) an analysis of the SEB components is given and the change characteristic of each component is analyzed to give insights into the processes controlling the mass balance at point scale as well as glacier scale.

2 Data and climatic settings

2.1 Study site and AWSs description

Chhota Shigri Glacier (32.28° N, 77.58° E) is a valley-type, non-surging glacier located in the Chandra-Bhaga river basin of Lahaul and Spiti valley, Pir Panjal range, Western Himalaya (Fig. 1). It lies ~ 25 km from the nearest city of Manali. This glacier feeds

TCD
8, 2867–2922, 2014

Chandra River, one of the tributaries of Indus river system. Chhota Shigri Glacier extends from 6263 to 4050 m a.s.l. with a total length of 9 km and area of 15.7 km^2 (Wagnon et al., 2007). The main orientation is north in its ablation area but its tributaries and accumulation area have a variety of orientations (Fig. 1). The lower ablation area (< 4500 m a.s.l.) is covered by debris representing approximately 3.4 % of the total surface area (Vincent et al., 2013). The debris layer is highly heterogeneous, from some millimeter silts to big boulders exceeding sometimes several meters. Its snout is well defined, lying in a narrow valley and giving birth to a single pro-glacial stream. The equilibrium line altitude (ELA) for a zero net balance is close to 4900 m a.s.l. (Wagnon et al., 2007). This glacier is located in the monsoon–arid transition zone and influenced by two different atmospheric circulation systems: the ISM during summer (July–September) and the Northern Hemisphere MLW during winter (January–April) (e.g., Bookhagen and Burbank, 2010).

Two meteorological stations (AWS1 and AWS2) have been operated on Chhota Shigri Glacier (Fig. 1). AWS1 was operated between 12 August 2012 and 4 October 2013, in the middle of ablation zone (4670 m a.s.l.) on an almost horizontal and homogeneous surface while AWS2 is located off-glacier on a western lateral moraine (4863 m a.s.l.) and functioning continuously since 18 August 2009. At AWS1 and AWS2, meteorological variables are recorded as half-hourly means with a 30 s time step, except for wind direction (half-hourly instantaneous values), and stored in a Campbell CR1000 data logger. AWS1 is equipped with a tripod standing freely on the glacier with wooden plates at its legs and sinks with the melting surface. AWS2 provides pluri-annual meteorological data (from 2009 to 2013) allowing characterization of the seasons as well as analysis of the local climatic conditions on Chhota Shigri Glacier. Both AWS1 and AWS2 were checked and maintained every month during the summers (accessibility in winter was not possible). At the glacier base camp (3850 m a.s.l.), an all-weather precipitation gauge with a hanging weighing transducer (Geonor T-200B) has been operating continuously since 7 July 2012 (Fig. 1). Geonor sensor is suitable for both solid

TCD
8, 2867–2922, 2014

and liquid precipitation measurements. Table 1 gives the list of meteorological variables used in this study, with their specifications.

2.2 Meteorological data

Only AWS1 data were used for SEB calculations. During winter, the lower sensors (T_{air}, RH, u) were buried under heavy snowfalls on 18 January 2013, and AWS1 stopped operating completely on 11 February 2013 till 7 July 2013 when the glacier was again accessible and AWS1 could be repaired. To ensure good data quality, the period between 4 and 11 February 2013 was eliminated as this period was supposed to be influenced by near surface snow. Thus, complete data set of 263 days in two separate periods (13 August 2012 to 3 February 2013 and 8 July to 3 October 2013) are available for analysis, except SR50A, for which data are also missing from 8 September to 9 October 2012. The records from AWS2 have very few data gaps (0.003 %, 0.29 %, and 0.07 % data gaps over the 4-year period for T_{air}, u and WD, respectively). These gaps were filled by linear interpolation using the neighboring data. Only one long gap exists for LWI data between 18 August 2009 and 22 May 2010.

In snow- and ice-melt models, cloud cover is investigated by computing "cloud factors", defined as the ratio of measured and modeled clear-sky solar radiation (Greuell et al., 1997; Klok and Oerlemans, 2002; Mölg et al., 2009). In the present study cloud factor is calculated by comparing SWI with solar radiation at the top of atmosphere (STOA) according to the Eq.: cloud factor = 1.3–1.4 × (SWI/STOA) that represents a quantitative cloud cover estimate. The values 1.3 (offset) and 1.4 (scale factor) were derived from a simple linear optimization process (Favier et al., 2004). The cloud factor is calculated between 11:00 to 15:00 local time (LT) to avoid the shading effect of steep valley walls during morning and evening time. The theoretical value of STOA is calculated for a horizontal plane following the Iqbal, (1983) and considering the solar constant equal to 1368 W m^{-2}.

TCD
8, 2867–2922, 2014

2.3 Accumulation and ablation data

The SR50A sensor records the accumulation of snow (height decrease of the sensor) or the melting of ice and melting or packing of snow (height increase) at 4670 m a.s.l. close to AWS1 (Fig. 2). This sensor does not involve an internal temperature sensor to compensate the variations in speed of sound as a function of T_{air}. Therefore, temperature corrections for the speed of sound were applied to the sensor output using T_{air} recorded at the higher level. Measured distance may reduce during the evening which could be misunderstood as a snowfall event (Maussion et al., 2011). In order to minimize this effect and to reduce the noise, a 3 h moving mean is applied to smooth the SR50A data. On Chhota Shigri Glacier, during summer-monsoon season, sporadic snowfall events and follow-up melting may occur within hours. Therefore, the sensor height variations from the 3 h smoothed SR50A data should be calculated over a time interval long enough to detect the true height changes during the snowfalls and short enough to detect a snowfall before melting begins. Given that SR50A measurements have uncertainty of ±1 cm, an agreement was achieved with a 6 h time step between smoothed SR50 data to get surface changes by more than 1 cm.

Point mass balance was measured from ablation stake no. VI which is located at the same elevation and around 20 m south to AWS1. Frequent measurements, with intervals of some days to a couple of weeks, were made at stake no. VI during summer expeditions. In summer 2012, 3 stake measurements, with intervals of 10 to 15 days, have been performed from 8 August to 21 September 2012 and in summer 2013, 6 measurements, with intervals of 7 to 30 days, have been carried out from 8 July to 3 October 2013. By subtracting the snow accumulation assessed from SR50A measurements at AWS1 (assuming a density of 0.2 for accumulated snow), the ablation was derived corresponding to every period between two stake measurements.

TCD
8, 2867–2922, 2014

2.4 Climatic settings

2.4.1 Characterization of seasons

In this section, the meteorological conditions on Chhota Shigri Glacier, as derived from the measurements at AWS2, are described. The Himalayan Mountains are situated in the subtropical climate zone, characterized by high annual thermal amplitude, that allows a separation into summer and winter seasons. The general circulation regime over Himalaya is controlled by the Inter-Tropical Convergence Zone (ITCZ) (Bookhagen and Burbank, 2006, 2010). On Chhota Shigri Glacier, a hydrological year is defined from 1 October to 30 September of following year (Wagnon et al., 2007). Figure 3 shows the mean annual cycle of monthly T_{air} and RH during the four hydrological years, from 1 October 2009 to 30 September 2013, recorded at AWS2. The standard deviations of mean monthly measurements were 7.0 °C and 13 % for T_{air} and RH, respectively, approving that on Chhota Shigri Glacier, T_{air} and RH variations are large enough to characterize pronounced seasonal regimes. A warm summer-monsoon season with high relative humidity from June to September and a cold winter season, comparatively less humid, from December to March were identified. Besides, a pre-monsoon season from April to May and a post-monsoon season from October to November could also be defined.

Daily mean T_{air} ranges between −22.0 and +7.3 °C with a mean T_{air} of −6.0 °C for the studied cycle (1 October 2009 to 30 September 2013), reflecting the high altitude of the AWS2 location (4863 m a.s.l.). The coldest month was January with the mean T_{air} of −15.8 °C and the warmest month was August with a mean T_{air} of 4.3 °C. Table 2 displays the mean seasonal values of all studied variables for the whole period (1 October 2009 to 30 September 2013). Summer-monsoon season is warm (annual mean T_{air} = 2.5 °C) and calm (annual mean u = 2.8 m s^{-1}) with high humidity (annual mean RH = 68 %), whereas the winter season is characterized with cold (annual mean T_{air} = −13.4 °C) and windy (annual mean u = 5.5 m s^{-1}) conditions with relatively less humidity (annual mean RH = 42 %). The mean annual RH is 52 %. An increase (decrease) in mean monthly RH in June (October) shows the onset (end) of mon-

TCD
8, 2867–2922, 2014

soon on Chhota Shigri Glacier. The highest mean monthly RH of summer-monsoon was observed in August (74 %) while in winter maximum was observed in February (51 %) (Fig. 3), confirming that Chhota Shigri Glacier is receiving moisture alternately from ISM during summer-monsoon and MLW during winter season. Pre-monsoon and post-monsoon seasons showed intermediate conditions for air temperature, moisture and wind speed (Table 2). Although during summer-monsoon season the solar angle is at its annual maximum, SWI is the highest during the pre-monsoon season with a mean value of 299 W m^{-2}. Indeed, in summer-monsoon SWI is reduced by 33 W m^{-2} (summer-monsoonal mean = 266 W m^{-2}) because of high cloud cover revealed by high moisture conditions (RH = 68 % with STD = 1 %, Table 2). The low values of SWI, during summer-monsoon season, are compensated by high values of LWI (Fig. 3 and Table 2) mostly emitted from warm summer-monsoonal clouds. Post-monsoon and winter seasons are rather similar, receiving low and almost same SWI (176 and 161 W m^{-2}, respectively) and LWI (187 and 192 W m^{-2}, respectively). The low SWI and LWI values over these seasons are mainly related to the decreasing solar angle (for SWI), and low values of T_{air}, RH and cloudiness (for LWI), respectively.

2.4.2 Influence of ISM and MLW

The whole Himalayan range is characterized by, from west to east, the decreasing influence of the MLW and the increasing influence of the ISM (Bookhagen and Burbank, 2010), leading to distinct precipitation regimes on glaciers depending on their location.

Figure 4 shows the monthly precipitations for a complete hydrological year between 1 October 2012 and 30 September 2013 at Chhota Shigri Glacier base camp (3850 m a.s.l.) (Fig. 1). Surprisingly, the months with minimum precipitation were July to November (mean value of 16 mm) and those with maximum precipitation were January and February (183 and 238 mm, respectively). For the ease of understanding, Wulf et al. (2010) divided the distribution of precipitation over the same region in two periods i.e. from May to October with precipitation predominantly coming from ISM and from November to April with precipitation coming from MLW. ISM contributed only 21 %

TCD
8, 2867–2922, 2014

while MLW added 79 % precipitation to the annual precipitation (976 mm) at Chhota Shigri base camp for 2012/2013 hydrological year. In Fig. 5, a comparison of 2012/2013 monthly precipitation at base camp is also done with long-term (1969–2013) mean monthly precipitations at Bhuntar meteorological station, Beas basin (Fig. 1). Although this station is only about 50 km from Chhota Shigri Glacier, the precipitation regime is noticeably different because ISM and MLW equally contribute to the average annual precipitation (916 mm yr^{-1}). The different precipitation regimes in this region can be explained by the location of the orographic barrier which ranges between 4000 and 6600 m in elevation (Wulf et al., 2010). ISM, coming from Bay of Bengal in the south-east, is forced by the orographic barrier to ascend that enhances the condensation and cloud formation (Bookhagen et al., 2005) thus, provides high precipitations in the windward side of the orographic barrier at Bhuntar meteorological station (51 % of the annual precipitation) and low precipitations in its leeward side at Chhota Shigri Glacier (21 % of annual precipitation). In contrast to the ISM, MLW moisture derived from the Mediterranean, Black, and Caspian seas is transported at higher tropospheric levels (Weiers, 1995). Therefore, the winter westerlies predominantly undergo orographic capture at higher elevations in the orogenic interior providing high precipitations at Chhota Shigri Glacier (79 % of annual precipitation) compared to Bhuntar meteorological station in windward side (49 % of annual precipitation). Thus, Chhota Shigri Glacier seems to be a winter-accumulation type glacier receiving most of its annual precipitation during winter season. This precipitation comparison between glacier base camp and Bhuntar meteorological station is only restricted to 2012/2013 hydrological year, when precipitation records at glacier base camp are available. Long-term precipitation data at glacier site are still required to better understand the relationship between both precipitation regimes occurring on the southern and northern slopes of Pir Panjal Range.

TCD
8, 2867–2922, 2014

2.4.3 Representativeness of 2012/2013 hydrological year

Given that long-term meteorological data at the glacier are unavailable, the representativeness of the meteorological conditions prevailing during the 2012/2013 hydrological year is assessed using T_{air} and precipitation data from the nearest meteorological station at Bhuntar. Figure 5a shows the comparison of 2012/2013 T_{air} with the long-term mean between 1969 and 2013 at seasonal as well as annual scale. T_{air} in 2012/2013 was systematically higher in all seasons (0.5 °C, 0.5 °C and 0.6 °C in winter, pre-monsoon and summer-monsoon seasons, respectively) except for post-monsoon season when it was lower (0.4 °C) than mean seasonal T_{air} over 1969–2013 period. At annual scale, 2012/2013 hydrological year was 0.4 °C warmer with T_{air} close to the 75th percentile of annual mean T_{air} between 1969 and 2013 period. Figure 5b compares the precipitation observed during the 2012/2013 hydrological year to the mean over the 1969–2013 period. In 2012/2013 hydrological year, both ISM (May to October) and MLW (November to April) circulations brought almost equal amount (49 and 51 %, respectively) of precipitation at Bhuntar meteorological station. This year the ISM precipitation was equal to mean ISM precipitation over 1969/2013 whereas MLW precipitation was 5 % higher than mean MLW precipitation over 1969/2013 hydrological years (Fig. 5b); therefore, the annual precipitation for 2012/2013 was found slightly higher (943 mm w.e.) than mean annual precipitation (919 mm w.e.) over 1969/2013 hydrological years. In conclusion, 2012/2013 hydrological year was relatively warmer with slightly higher precipitation compared to annual means over 1969–2013 period but can be considered as an average year.

TCD
8, 2867–2922, 2014

3 Methodology: SEB calculations

3.1 SEB equation

The meteorological data from AWS1 were used to derive the SEB at point-scale. A unit volume of glacier is defined from the surface to a depth where no significant heat fluxes are found. On this volume, for a unit of time, and assuming a lack of horizontal energy transfers, the SEB Eq. can be expressed as (e.g., Oke, 1987, p. 90):

$$\mathrm{SWI} - \mathrm{SWO} + \mathrm{LWI} - \mathrm{LWO} + H + \mathrm{LE} + G + P = Q \quad (1)$$

where SWI, SWO, LWI and LWO are the incident short-wave, outgoing short-wave, incoming long-wave and outgoing long-wave radiations, respectively. H and LE are the sensible and latent turbulent heat fluxes, respectively. G is the conductive heat flux in the snow/ice and P is the heat supplied by precipitation. Q is the net heat flux available at glacier surface. All the fluxes ($\mathrm{W\,m^{-2}}$) towards the surface are taken as positive and vice-versa. The heat supplied by precipitation on glaciers is insignificant compared to the other fluxes (Oerlemans, 2001) therefore neglected here. The conductive heat transfer within the snowpack or the ice is also ignored as it tends to be small when compared to radiative or turbulent fluxes (Marks and Dozier, 1992). Consequently the SEB is described by the sum of radiation fluxes and turbulent heat fluxes.

The model calculates the SEB at point scale according to Eq. (1) at a half-hourly time-step. When surface temperature (T_{surf}) reaches the melting point, the amount of melt M (m w.e.) is calculated from Q divided by the latent heat of fusion ($3.34 \times 10^5\,\mathrm{J\,kg^{-1}}$) and the density of water ($1000\,\mathrm{kg\,m^{-3}}$). T_{surf} was derived from LWO using the Stefan–Boltzmann equation assuming that the emissivity of the ice/snow is unity ($\mathrm{LWO} = \sigma T_{\mathrm{s}}^4$ with $\sigma = 5.67 \times 10^{-8}\,\mathrm{W\,m^{-2}\,K^{-4}}$) and that it cannot exceed 273.15 K. Here it is considered that the surface is in melting conditions when T_{surf} reaches 0 °C.

TCD
8, 2867–2922, 2014

3.2 Radiative fluxes

Radiation fluxes are directly measured in the field (Table 1) however several corrections were applied to this data before using in SEB model. Night values of SWI and SWO were set to zero. SWI is found much more sensitive to measurement uncertainties compared to SWO (Van den Broeke et al., 2004). At high elevation sites, such as Himalaya, measured SWO can be higher than SWI (2.6 % of total data here) during the morning and evening time when the solar angle is low because of poor cosine response of the upward-looking radiation (SWI) sensor (Nicholson et al., 2013). Besides, as AWS1 was installed on the middle of the ablation area, the unstable glacier surface during ablation season conceivably give rise to a phase shift by mast tilt (Giesen et al., 2009). However in these conditions, SWO sensor is slightly affected because it is receiving isotropic radiation mostly. SWI is calculated from SWO (raw) and accumulated albedo (α_{acc}) to elude the impact of the phase shift because of tilting during the daily cycle of SWI and poor cosine response of the SWI sensor during the low solar angles. α_{acc} values were computed (Eq. 2) as the ratio of accumulated SWO (raw) and SWI (raw) over a time-window of 24 h centered on the moment of observation using the method described in Van den Broeke et al. (2004). The obvious shortcoming of the accumulated albedo method is the elimination of the clear-sky daily cycle in α_{acc} (Van den Broeke et al., 2004).

$$\alpha_{acc} = \frac{\sum_{24} \mathrm{SWO}}{\sum_{24} \mathrm{SWI}} \quad (2)$$

A correction has also been applied to long-wave radiations as the air particles between the glacier surface and CNR-4 sensor radiates and influences the LWI (underestimation of LWI at the surface) and LWO (overestimation). This generally occurs when T_{air} is higher than 0 °C during summer-monsoon season (July to September). Figure 3a reveals a linear relation between LWO and T_{air} above 0 °C. Measured LWO was often found substantially greater than 315.6 W m^{-2}, which is the maximum possible value for

TCD
8, 2867–2922, 2014

a melting glacier surface. Therefore, a correction can be done using LWO. We adopted the method described by Giesen et al. (2014) and fitted a linear function to the median values of the additional LWO (greater than 315.6 W m^{-2}) for all 0.5 °C T_{air} intervals above 0 °C, assuming that the correction is zero at 0 °C. This correction was added to LWI and subtracted from LWO (Fig. 6b) when T_{air} was higher than 0 °C. Corrections have half-hourly values up to 22 W m^{-2} for T_{air} of 11 °C. Over all half-hourly periods with T_{air} above 0 °C, the average correction was 6.3 W m^{-2}.

3.3 Turbulent fluxes

3.3.1 Turbulent flux calculations

Although u, T_{air} and RH were measured at two levels (0.8 and 2.5 m) at AWS1, the bulk method is used to calculate the turbulent heat fluxes. Denby and Greuell (2000) showed that the bulk method gives reasonable results in the entire layer below the wind speed maximum even in katabatic wind conditions whereas the profile method severely underestimates these fluxes. In turn, the bulk method has already been applied in various studies where katabatic winds dominate (e.g. Klok et al., 2005; Geisen et al., 2014). The major characteristic of katabatic flow is the wind speed maximum which is dependent on glacier size, slope, temperature, surface roughness and other forcing mechanisms (Denby and Greuell, 2000). At AWS1 site, u at the upper level (initially at 2.5 m) is always higher (99.6 % of all half-hourly data) than that at the lower level (initially at 0.8 m) suggesting that the wind speed maximum is almost systematically above 2.5 m and justifies the choice of the bulk method.

The bulk method calculates the turbulent fluxes including stability correction. This method is usually used for practical purposes because it allows the estimation of the turbulent heat fluxes from one level of measurement (Arck and Scherer, 2002). In this approach, a constant gradient is assumed between the level of measurement and the surface; consequently, surface values have to be evaluated. The stability of the surface layer is described by the bulk Richardson number, Ri_b (Eq. 3) which relates the relative

TCD
8, 2867–2922, 2014

effects of buoyancy to mechanical forces (e.g., Brutsaert, 1982; Moore, 1983; Oke, 1987):

$$\mathrm{Ri_b} = \frac{g\frac{(T_{\mathrm{air}}-T_{\mathrm{surf}})}{(z-z_{0\mathrm{T}})}}{T_{\mathrm{air}}\left(\frac{u}{z-z_{0\mathrm{m}}}\right)^2} = \frac{g(T_{\mathrm{air}}-T_{\mathrm{surf}})(z-z_{0\mathrm{m}})^2}{T_{\mathrm{air}}u^2(z-z_{0\mathrm{T}})} \quad (3)$$

where z is the level of measurements. T_{air} and u are used from the upper level that provides a longer period for investigation. The sensors height was extracted from SR50A records except a data gap between 8 September to 9 October 2012. Over this period sensors height were assumed to be constant and set as 2.5 m being AWS1 in free standing position. g is the acceleration of gravity ($g = 9.81\,\mathrm{m\,s^{-2}}$), T_{surf} is the surface temperature (in K). $z_{0\mathrm{m}}$ and $z_{0\mathrm{T}}$ are the surface roughness parameters (in m) for momentum and temperature, respectively. Assuming that local gradients of mean horizontal u, mean T_{air} and mean specific humidity q are equal to the finite differences between the measurement level and the surface, it is possible to give analytical expressions for the turbulent fluxes (e.g., Oke, 1987):

$$H = \rho\frac{C_P k^2 u(T_{\mathrm{air}}-T_{\mathrm{surf}})}{\left(\ln\frac{z}{z_{0\mathrm{m}}}\right)\left(\ln\frac{z}{z_{0\mathrm{T}}}\right)}(\Phi_{\mathrm{m}}\Phi_{\mathrm{h}})^{-1} \quad (4)$$

$$\mathrm{LE} = \rho\frac{L_S k^2 u(q-q_{\mathrm{surf}})}{\left(\ln\frac{z}{z_{0\mathrm{m}}}\right)\left(\ln\frac{z}{z_{0\mathrm{q}}}\right)}(\Phi_{\mathrm{m}}\Phi_{\mathrm{v}})^{-1} \quad (5)$$

where ρ is the air density (in $\mathrm{kg\,m^{-3}}$) at 4670 m a.s.l. at AWS1 and calculated using ideal gas equation ($\rho = \frac{P_{\mathrm{atm}}}{R_a T}$, where R_{a} being the specific gas constant for dry air and P_{air} is given by the measurements and around 565 hPa). C_P is the specific heat capacity for air at constant pressure ($C_p = C_{\mathrm{pd}}\,(1 + 0.84q)$ with $C_{\mathrm{pd}} = 1005\,\mathrm{J\,kg^{-1}\,K^{-1}}$, the specific

TCD
8, 2867–2922, 2014

heat capacity for dry air at constant pressure), k is the von Karman constant ($k = 0.4$) and L_s is the latent heat of sublimation of snow or ice ($L_s = 2.834 \times 10^6\,\mathrm{J\,kg^{-1}}$). Furthermore, q is the mean specific humidity (in $\mathrm{g\,kg^{-1}}$) of the air at the height z and q_{surf} is the mean specific humidity at surface. z_{0T} and z_{0q} are the surface roughness parameters for temperature and humidity, respectively. To compute turbulent fluxes Eqs. (4) and (5), it is assumed that the temperature is equal to T_{surf} at z_{0T} and that the air is saturated with respect to T_{surf} at z_{0q}. The last assumption helps to calculate surface specific humidity q_{surf}. The non-dimensional stability functions for momentum (Φ_m), for heat (Φ_h) and moisture (Φ_v) can be expressed in terms of $\mathrm{Ri_b}$ (e.g., Favier et al., 2011):

For $\mathrm{Ri_b}$ positive (stable): $(\Phi_m\Phi_h)^{-1} = (\Phi_m\Phi_v)^{-1} = (1 - 5\mathrm{Ri_b})^2$ (6)

For $\mathrm{Ri_b}$ negative (unstable): $(\Phi_m\Phi_h)^{-1} = (\Phi_m\Phi_v)^{-1} = (1 - 16\mathrm{Ri_b})^{0.75}$ (7)

The lower and upper limits of $\mathrm{Ri_b}$ were fixed at −0.4 and 0.23, respectively beyond that all turbulence is suppressed (Denby and Greuell, 2000; Favier et al., 2011).

3.3.2 Roughness parameters

The aerodynamic (z_{0m}) and scalar roughness lengths (z_{0T} and z_{0q}) play a pivotal role in bulk method as the turbulent fluxes are very sensitive to the choice of these surface roughness lengths (e.g., Hock and Holmgren, 1996; Wagnon et al., 1999). In several studies (e.g., Wagnon et al., 1999; Favier et al., 2004), the surface roughness lengths were all chosen equal ($z_{0m} = z_{0T} = z_{0q}$) and used as calibration parameters. In the present study, the z_{0m} was calculated assuming a logarithmic profile for wind speed between both the levels of measurements in neutral conditions (e.g., Moore, 1983):

$$z_{0m} = \exp\left(\frac{u_2 \ln z_1 - u_1 \ln z_2}{u_2 - u_1}\right) \quad (8)$$

where u_1 and u_2 are the wind velocities measured at the lower and higher levels z_1 and z_2, respectively. For $-0.005 < \mathrm{Ri_b} < 0.005$ (11 % of our total data set, at half-hourly

TCD
8, 2867–2922, 2014

time-step), it was assumed that conditions are neutral, and half-hourly values for z_{0m} were calculated using the Eq. (8). Half-hourly values of z_{0m} were assessed separately for ice and snow surfaces, based on field observations (snow covered surface between 16 September 2013 and 17 January 2013 and ice-covered surface the rest of the time). The z_{0m} was calculated as 0.016 m (with STD of 0.026 m) and 0.001 m (0.003 m) for ice and snow surfaces, respectively. During summer-monsoon, the surface is covered with hummocks and gullies and z_{0m} is large whereas in winter, snow covers all surface irregularities and fills up the gullies (Fig. 2) providing small values of z_{0m}. The ratio between roughness lengths (z_m/z_q and z_m/z_T) depends on the Reynolds number of the flow according to Andreas (1987) polynomials. For high Reynolds numbers (aerodynamically rough flows), the polynomials suggested by Smeets and Van den Broeke (2008) for hummocks were used. The respective mean values obtained for z_T and z_q are identical and equal to 0.004 m over ice surfaces, and 0.001 m over snow surfaces. These values are similar to z_{0m} values for snow-smooth surfaces as already observed by Bintanja and Van den Broeke (1995) and lower for icy-rough surfaces as pointed out by many authors (e.g., Andreas, 1987; Hock and Holmgren, 1996; Meesters et al., 1997).

4 Results

4.1 Analysis of the meteorological conditions at AWS1

In order to understand the seasonal evolution of the physical processes controlling the mass balance of the glacier, different representative periods for various seasons were selected. The selected representative periods are post-monsoon (1 October 2012 to 29 November 2012), winter (1 December 2012 to 29 January 2013) and summer-monsoon (8 July 2013 to 5 September 2013). The selection of these representative periods was based on the meteorological conditions observed in Sect. 2.4 and available dataset at AWS1. The same length of 60 days of each representative period was chosen for

TCD
8, 2867–2922, 2014

justified comparison among different seasons. Unfortunately data was not available for pre-monsoon season. Measurements (T_{air}, RH, u and WD) recorded at the upper level sensors were used for the analysis, since the records from the lower level sensors have longer data gap because of early burial of sensors. A summary of the mean variables measured in different representative periods at AWS1 is given in Table 3.

Figure 7 shows the daily averages of T_{air}, u, RH, LWI, LWO, SWI, SWO, STOA, cloud factor, α_{acc} and snow falls for all three representative periods. The meteorological variables show strong seasonality and day-to-day variability. The last panels of Fig. 7 represent the daily snowfall amounts (with a data gap between 1 and 8 October 2012) at AWS1 site extracted from SR50A data (by applying a fresh snow density of 200 kg m^{-3}). Post-monsoon and winter periods are cold with mean T_{air} and T_{surf} always far below freezing point (Fig. 7 and Table 3). During post-monsoon period mean u and α_{acc} progressively increased (mean u = 4.7 m s^{-1} and α_{acc} = 0.73) and reached their highest values in winter period (mean u = 4.9 m s^{-1} and α_{acc} = 0.79). α_{acc} remains almost constant in winter period showing the persistent snow cover. Snowfalls in post-monsoon period were frequent but generally very light (< 10 mm w.e.), whereas winter period received a substantial amount of snow (the heaviest snowfalls were observed on 16 December 2012, and 17, 18 January 2013 with 32, 44 and 80 mm w.e., respectively). These snowfall events are associated with high RH, α_{acc}, cloud factor and LWI. Obviously, an abrupt decrease of SWI (consequently low SWO) is noticed during snowfall events. Most of the time, due to very cold and dry high-elevation atmosphere, LWI remains very low during both periods, with mean values of 205 and 189 W m^{-2} in post-monsoon and winter periods, respectively (Table 3). An analysis of Fig. 7 showed that overcast days with high cloud factor, high RH, increased LWI and decreased SWI are evident during all three representative periods.

Summer-monsoon period is hot and calm with relatively high humidity (Fig. 7 and Table 3). SWI is the highest during summer-monsoon period with a mean value of 248 W m^{-2} (Table 3). Most of the part (81 %) of SWI is absorbed by the glacier surface because of the lowest values of α_{acc} (mean value = 0.19) consequently low SWO. The

TCD
8, 2867–2922, 2014

low and almost constant α_{acc} indicates that the glacier ice was exposed all the time. During summer field expeditions the cloud formation in afternoon hours can often be observed. The surface remains almost permanently in melting conditions, as shown by constantly maximal LWO values. Although the summer-monsoon period is characterized by the highest values of RH (82 %) and cloud factor (0.4), little snowfall events are observed from the SR50A at AWS1 site. Given that T_{air} was above freezing point, the precipitation might have been occurred in the form of rain most of the time. Due to warm, humid and cloudy conditions, LWI is much higher in summer-monsoon than during the other seasons, with a mean value of 300 W m^{-2} (Table 3).

Post-monsoon and winter periods are characterized by high winds (mean u values of 4.7 and 4.9 m s^{-1}, respectively; Table 3). In summer-monsoon period u is quite stable (STD = 0.5 m s^{-1}) and gusts at minimum strength with a mean value of 3.6 m s^{-1}. Chhota Shigri Glacier is situated in an almost north-south oriented valley and the AWS1 site is surrounded by steep valley walls from east and west directions (Fig. 1). The scatter plots of u with T_{air} and WD over all of the observation periods at half-hourly time scale were plotted following Oerlemans (2010). Figure 8a mostly shows a linear relationship between T_{air} above melting point and u at AWS1 site showing that increasing u is associated with increasing near-surface T_{air}, indicative of katabatic forcing whereas Fig. 8b reveals a mean down-glacier wind (WD of 200–210°) most of the time.

Although, generally, katabatic wind flow is more expected during summer season than in winter (Oerlemans, 2010), Fig. 9 shows that this is not the case at AWS1 on Chhota Shigri Glacier. WD, measured at AWS1, indicates that there is a persistent down-glacier wind coming from south to southwest (200–210°) during post-monsoon and winter periods. In winter the half-hourly mean u reaches up to 10 m s^{-1} compared to 8 m s^{-1} in post-monsoon period. During both post-monsoon and winter periods the glacier surface is snow covered (with high α_{acc}, Fig. 7) and a down-glacier wind is maintained by the negative radiation budget (Sect. 4.2) of the snow surface which gives rise to cooling to the near-surface air, generating katabatic flow (Grisogono and

TCD
8, 2867–2922, 2014

Oerlemans, 2002). Occasionally, wind from south-east (160°) in the direction of a large hanging glacier was also observed.

Further, on Chhota Shigri Glacier, in summer-monsoon period the wind regime is quite remarkable. A down-glacier wind as a result of katabatic forcing, coming from south to southwest (200–210°) is relatively weak in summer-monsoon period. Wind also tends to come from south-east (160°), in the direction of a large hanging glacier (Fig. 1). The upcoming valley wind coming from north-east (50°), blowing against the katabatic wind, is weak at the AWS1 site and appears only during summer-monsoon periods when the katabatic wind is comparatively weak. As a cumulative result of valley and katabatic winds, a wind from 110° is also observed. AWS1 is surrounded by the steep valley walls and probably the impact of synoptic wind remains feeble thus the katabatic flow is the dominated phenomenon most of the time of the year, which is typical for many glaciers (Van den Broeke, 1997).

4.2 Mean values of the SEB components

Mean SEB values for three representative periods are presented in Fig. 10 and are reported in Table 3. The results indicate that the SWN is highly variable from a low winter mean value of 29 W m^{-2} to a very high summer-monsoon mean value of 202 W m^{-2} (Table 3). Besides the seasonal changes in sun inclination, the main reason for the seasonal variability of SWN is the contrast in surface albedo in different periods (Table 3). Seasonal variations in LWN are rather low, post-monsoon and winter periods show minimum values of LWN (mean = −57 and −49 W m^{-2}, respectively) while a maximum value was reached in summer-monsoon period (mean = −13 W m^{-2}) when relatively high T_{surf} (mean = −0.1 °C) coincides with warm and humid conditions, associated with intense cloud covers leading to high values of LWI. The net radiation heat flux R (SWN + LWN) was negative in post-monsoon and winter periods, giving rise to near-surface air cooling, with mean values of −9 and −20 W m^{-2}, respectively whereas in summer-monsoon, it was the main heat source with a mean value of 188 W m^{-2}. During all representative periods, the atmosphere transported heat towards the glacier

TCD
8, 2867–2922, 2014

surface in the form of H. The highest contribution of H (associated with the highest u, Table 3) was in winter with a mean value of 33 W m^{-2} (Table 3). LE was continuously negative in post-monsoon and winter periods with mean values of −25 and −20 W m^{-2}, respectively. Therefore, surface losses mass through sublimation (corresponding to respective mean daily rates of 0.8 and 0.6 mm w.e. d^{-1}). However, in summer-monsoon period, a sign shift in LE from negative to positive occurred. The relatively high T_{air} and RH (Table 3) lead to a reversal of the specific humidity gradient and therefore a positive LE for a melting valley glacier (Oerlemans, 2000). Because of this positive LE, glacier gained mass through condensation or re-sublimation (0.3 mm w.e. d^{-1}) of moist air at the surface (Table 3).

As a result of SEB, positive melt heat flux (Q), with almost the same oscillation trend as SWN (Fig. 10), occurred only in summer-monsoon period when melting conditions were prevailing all the time, leading to a mean daily melt rate of 60.9 mm w.e. d^{-1}. During summer-monsoon period SWN accounted for 88 % of the total heat flux and was the most important heat-flux component for surface melting. R was estimated as 82 % of the total heat flux that was complimented with turbulent sensible and latent heat fluxes with a share of 13 % and 5 %, respectively. During post-monsoon period the glacier started cooling down (mean Q = −4 W m^{-2}) and only a little melting (mean daily rate of 0.7 mm w.e. d^{-1}) occurred during the noon hours only, when occasionally T_{surf} reached 0 °C, while in winter period the glacier was too cold to experience any melting (mean Q = −7 W m^{-2}).

4.3 Model validation

The model provides a heat transfer at half-hourly time step to the glacier superficial layers that can be turned into melt when surface temperature is at 0 °C. Other possible way to lose/gain mass is from sublimation/condensation or re-sublimation. The amount of sublimation/condensation or re-sublimation (m w.e.) is computed from calculated LE dividing by the latent heat of sublimation (2.834×10^6 J kg^{-1}) and the density of water (1000 kg m^{-3}) if the half-hourly mean LE flux were found negative/positive. To validate

TCD
8, 2867–2922, 2014

the SEB model, computed ablation (melt + sublimation) was compared with the ablation measured at stake no. VI in the field (Sect. 2.3). The correlation between computed ablation from the SEB Eq. and measured ablation at stake no. VI is strong (r^2 = 0.98, n = 9 periods) indicating the robustness of the model. However, the computed ablation is 1.10 times higher than the measured one (Fig. 11), but this difference (10 % overestimation) is acceptable given the overall uncertainty of 140 mm w.e. in stake ablation measurements (Thibert et al., 2008). The SEB model can, therefore, generate an acceptable computation of point mass balance.

4.4 Mean diurnal cycle of the meteorological variables and SEB components

The mean diurnal cycles of the meteorological variables and SEB components for all three representative periods are shown in Fig. 12. Mean diurnal cycles of T_{surf} (equivalent to LWO) and T_{air} showed that the glacier was in freezing conditions during post-monsoon and winter periods all the time (Fig. 12) while in summer-monsoon T_{surf} is always at melting point in agreement with consistent positive T_{air}. Occasionally, for some days, half-hourly mean T_{air} (not shown here) may drop below freezing point during night in summer-monsoon and go above freezing point during noon hours in post-monsoon period. A wind speed maximum is observed in the afternoon hours during all the representative periods, which is consistent with T_{air}. This is a common phenomenon on valley glaciers, u increases in the afternoon (e.g., Van den Broeke, 1997; Greuell and Smeets, 2001) as a consequence of an increased glacier wind due to a stronger T_{air} deficit in the afternoon.

For all the representative periods, R is negative at night (indicating long-wave radiative cooling of the surface) and positive during day time. However, during the summer-monsoon period the night values of R are slightly less negative as the radiative cooling is attenuated due to enhanced RH, T_{air} and cloudiness, in turn high LWI. In daytime, R is much higher during the summer-monsoon than other periods, mainly because of exposed low-albedo ice at the glacier surface enhancing the absorption of solar radiation which is already high due to annual maximum of the solar angle.

TCD
8, 2867–2922, 2014

H and LE show similar trends in post-monsoon and winter periods. In the night, H remains permanently high ($\sim 50\,W\,m^{-2}$) and starts decreasing in the morning as the surface is heated up with R (Fig. 12). This daily cycle of H is in agreement with the daily cycle of Ri_b, showing stable conditions almost all day long ($Ri_b > 0$ except 4 h in the middle of the afternoon in winter), with very stable conditions in the night, and moderately stable during the day or even unstable in the afternoon in winter. LE is slightly negative in the night, decreases in the morning and shows the minimum values during early afternoon hours which are in agreement with increasing wind speed and stronger vertical gradients of specific humidity in the vicinity of the surface. During summer-monsoon, both H and LE are positive (heat supplied to the surface) and follow a similar trend, but H attains its peak approximately 2 h before LE. H shows a peak at ~14:00 LT with positive T_{air} and wind speed maximum (Fig. 12) whereas LE remains close to $0\,W\,m^{-2}$ until noon and increases with an afternoon wind speed maximum. The stability of the surface boundary layer is not very different from that observed during the other periods, highly stable at night, but moderately stable during the day due to the occurrence of warm up-valley winds blowing over a melting surface in summer-monsoon. Thus, LE is positive during summer-monsoon giving rise to condensation or re-sublimation in afternoon and early night hours.

During post-monsoon and winter periods, in the night and even during afternoon hours in winter, Q is negative, and a cold front penetrates into the superficial layers of the glacier. However, Q is rather low as R is mostly compensated by $H + LE$ except during noon hours when Q switches to slightly positive values. Heat is then transferred during a few hours of the day to the ice/snow pack whose temperature rises but not enough to reach melting conditions (T_{surf} remains below 0 °C) (Fig. 12). During summer-monsoon period, Q follows the diurnal cycle of R providing energy up to $740\,W\,m^{-2}$ to the glacier surface at around 13:00 LT. This energy is consumed for melting process as the surface is in melting conditions permanently (Fig. 12). Unfortunately, the dataset does not cover the pre-monsoon season. But during this season, the heat transferred to the glacier progressively increases as net short-wave radiation enhances in agreement

TCD
8, 2867–2922, 2014

with the rise of the solar angle, as well as the decreasing surface albedo. This heat is first used to warm up the surface layers of the glacier until T_{surf} reaches 0 °C, then melting starts.

5 Discussion

5.1 Control of summer-monsoon snowfalls on melting

Changes in the Asian monsoon climate and associated glacier responses have become predominant topics of climate research in High Asia Mountains (e.g., Mölg et al., 2012). Previously, based on a degree-day approach, Azam et al. (2014) suggested that winter precipitation and summer temperature are almost equally important drivers controlling the mass balance pattern of Chhota Shigri Glacier. Here this topic is addressed by analyzing the glacier melting on Chhota Shigri Glacier with summer-monsoon precipitations using more detailed SEB approach. Based on the available dataset, we selected the same length of summer-monsoon period (15 August to 30 September) from 2012 and 2013 years to compare the evolution of the computed cumulative melting (Fig. 13). Given that the SR50A at AWS1 site has a data gap between 8 September to 9 October 2012 and that this sensor cannot record rain events, daily precipitations, collected at glacier base camp (3850 m a.s.l.), are used in this analysis. These precipitations can be considered as rain (snow) at AWS1 site when T_{air} at AWS1 is above (below) 1 °C (e.g., Wagnon et al., 2009). In summer-monsoon 2012 Chhota Shigri Glacier received one important snowfall on 17–19 September of 25 mm w.e. (equivalent to 125 mm of fresh snow applying a density of 200 kg m^{-3}). This snowfall abruptly changed the surface conditions by varying the surface albedo from 0.19 to 0.73 (Fig. 13a). Therefore, the energy Q available at the glacier surface suddenly dropped from 125 W m^{-2} on 16 September to 14 W m^{-2} on 17 September as shown by the sharp change in the melting rate (slope of the melting curve on Fig. 13a) associated to this specific snowfall event. The effect is also evident on T_{surf} evolution.

TCD
8, 2867–2922, 2014

The daily number of hours with $T_{surf} > -1\,^{\circ}C$ decreased from 24 to 6 h and remained around this value showing that melting, continuous before the snowfall event, is, after, reduced to a few hours of the day. During the summer-monsoon 2013, the situation was different as the snowfalls were more sporadic and never big enough to efficiently slow down the melting. Consequently, a shift in the slope in the melting curve is not observed as was the case in mid-September 2012. Indeed, the light snowfalls, observed from 13 to 16 September 2013 and from 24 to 30 September 2013, were only able to protect the glacier from high melting for some days but could not maintain a persistent snow cover as in mid-September 2012. Ice was again exposed at the surface as revealed by low albedo values (~ 0.38) observed again a few days after the snowfalls. Mean T_{air} and the daily number of hours with $T_{surf} > -1\,^{\circ}C$ again rose up hence high melting was maintained. As a consequence, at point scale, although the cumulative melting between 15 August and 30 September was similar in 2012 and 2013 (1.92 and 1.94 m w.e., respectively), the main difference comes from the distribution of the melting along the considered period. In 2012, melt rates were higher during the first 31 days than in 2013 but an early snowfall efficiently slowed down the melting, although it was slightly less intense but more regular in 2013. This analysis highlights the role of snowfall events during the summer-monsoon season those play a key role on albedo and, in turn, on melting. This effect has already been described in other parts of the world. Sicart et al. (2011) suggested that melting on Zongo Glacier, Bolivia is reduced by wet season snowfalls via the albedo effect during the melt season. On Zhadang Glacier (central Tibetan Plateau) Zhang et al. (2013) indicated that the glacier surface mass balance was closely related to summer-monsoon precipitation seasonality and phase (snow vs. rain).

In order to investigate the impact of summer-monsoon snowfalls on glacier-wide mass balance, the annual glacier-wide mass balances between 2002 and 2013 were compared with the largest summer-monsoon daily snowfalls of the corresponding season. These snowfalls have been extrapolated using daily precipitation data from Bhuntar meteorological station (1092 m a.s.l.), assuming no precipitation gradi-

TCD
8, 2867–2922, 2014

ent and applying the daily lapse rate between Bhuntar and glacier calculated by Azam et al. (2014) with the idea that if the precipitation is in the form of snow (threshold temperature equal to 1 °C) at 4400 m a.s.l. (below 4400 m a.s.l. glacier is totally debris cover), the whole glacier is covered by summer-monsoonal snow.

The best relationship is obtained when considering the sum of the three most important daily snowfall records of the corresponding summer-monsoon season (Fig. 14). The correlation is strong (r^2 = 0.88, n = 11 years) and suggests that summer-monsoon snowfall events play a key role to control the mass balance of the glacier. Such snowfalls cover the whole glacier implying the albedo of the whole ablation area to suddenly switch from low to high values (ice to snow surfaces). Consequently, melting is abruptly reduced or even stopped at the glacier surface for several weeks or even for the rest of the ablation season that usually ends around mid-October in years without such strong summer-monsoon snowfalls. Thus, the intensity of such summer-monsoon snowfalls is among the most important drivers controlling the annual mass balance of Chhota Shigri Glacier.

Azam et al. (2014), using a degree-day approach, showed that winter precipitation and summer temperature are equally important drivers controlling the glacier-wide mass balance of Chhota Shigri Glacier. This present analysis extends this knowledge a step further, showing that summer-monsoon snowfalls also play an important role in controlling the annual mass balance of Chhota Shigri Glacier. Indeed, summer-monsoon air temperature is as crucial as summer precipitation mainly because it controls the amount of rain vs. snow received at the glacier surface and in turn, has an important control on glacier albedo and thus on the amount of short-wave radiation absorbed by the glacier surface which is the main heat source for Himalayan glaciers.

5.2 Comparison of the SEB of Chhota Shigri Glacier with that of other High Asia Mountain glaciers

In this section some key features of the energy fluxes responsible for the ablation on glaciers in High Asia Mountain are discussed in the light of the SEB results obtained

TCD
8, 2867–2922, 2014

on Chhota Shigri Glacier, as well as from some previously published studies. Table 4 shows an up-to-date compilation of SEB studies from High Asia Mountain glaciers coming from ablation zones of different glaciers during summer ablation periods.

As already highlighted on High Asia Mountain glaciers (Yang et al., 2011; Mölg et al., 2012; Zhang et al., 2013; Sun et al., 2014), the present study also showed that SWN is the largest source of energy to the glacier surface and mainly controls the temporal variability of melting whereas LWN is the greatest energy loss, moderate during the summer-monsoon season when LWO is almost compensated by maximum LWI due to warm, humid and cloudy atmosphere, and high during the rest of the year when LWI reaches minimum values (Fig. 10 and Table 3). SWN is inversely dependent on surface albedo. At AWS1 site on Chhota Shigri Glacier, during summer-monsoon period, precipitation often occurs in liquid form and surface albedo is relatively constant (Fig. 7). During such conditions SWN is driven by cloud factor (Fig. 7). However when precipitation occurs in solid phase (Fig. 13) the surface albedo abruptly changes and controls the SWN and in turn, melting. Sum of SWN and LWN, R, provides > 80 % energy flux to the glacier surface during summer-monsoon season for all High Asia Mountain glaciers (Table 4).

All the studied sites, described in Table 4, are on the debris free ablation area. Sensible turbulent heat flux is always positive and provides energy to the glacier surface, complimenting net radiation flux. However its contribution to R ranges from 7 % on Laohugou Glacier No. 12, western Qilian, China, to the maximum of 23 % on Zhadang Glacier, central Tibetan Plateau over the corresponding observation periods (Table 4). During the summer-monsoon season, LE is positive on Chhota Shigri Glacier due to warm and humid air at the glacier surface, giving rise to condensation or re-sublimation at the surface. Such phenomenon has already been observed on AX010 Glacier located in an ISM-dominated region, Central Himalaya, Nepal, where Kayastha et al. (1999) measured a positive LE between 25 May and 25 September 1978 in the ablation area. On Parlung Glacier No. 4, southeast Tibetan Plateau, however, the mean LE was slightly negative over 21 May to 8 September 2009 (Table 4), it was continu-

TCD
8, 2867–2922, 2014

ously positive with a mean value of 8 W m^{-2} during the core summer-monsoon season between 25 June and 21 August 2009 because of considerably high temperature and relative humidity coming with the summer-monsoon circulation over this period (Table 2 in Yang et al., 2011). Conversely, in the central Tibetan Plateau, where dry conditions prevail, on Zhadang Glacier, LE is continuously negative at monthly scale (Mölg et al., 2012) but at daily time scale it was slightly positive during the core monsoon-season for a few days when the air temperature and relative humidity were the highest (Figs. 2 and 5 in Zhang et al., 2013). Sun et al. (2014) also showed that on Laohugou Glacier No. 12, Western Qilian Mountains, LE is negative throughout the summer season (1 June to 30 September 2011), and rarely becomes positive (only on 2 and 3 July). Similarly on Xixibangma Glacier, south central Tibetan Plateau, and Keqicar Glacier, southwest Tianshan, LE is found negative during all the observation period, thus sublimation. From present analysis (Table 4), it can be surmised that, on High Asia Mountain glaciers, sublimation predominates in summer-monsoon season over the ablation zone of the glaciers which are less affected by the ISM and submitted to drier conditions than those directly affected like Chhota Shigri Glacier, where LE brings a significant amount of energy at the glacier surface, in the form of condensation/re-sublimation.

6 Conclusion

At 4863 m a.s.l. on a lateral moraine of Chhota Shigri Glacier (AWS2), the meteorological dataset since August 2009 is one of the longest ever recorded datasets at high elevation in the Indian Himalaya where meteorological observations are short and scarce. Mean monthly meteorological conditions at AWS2 show large month-to-month variability. A warm and calm summer-monsoon season with high relative humidity from June to September and a cold and windy winter season with comparatively less humidity from December to March were identified. Besides, a pre-monsoon season from April to May and a post-monsoon season from October to November with intermediate conditions were also defined. Precipitation records at glacier base camp suggest that Chhota Shi-

TCD
8, 2867–2922, 2014

gri Glacier is a winter accumulation type glacier receiving around 80 % of its annual precipitation from MLW in winter and 20 % from ISM, but longer precipitation records at glacier site are still needed to confirm this feature.

A physically-based energy balance experiment was carried out to understand the melting processes on Chhota Shigri Glacier using the forcing data, over two separate periods from 13 August 2012 to 3 February 2013 and from 8 July to 3 October 2013, recorded at an in-situ meteorological station (AWS1, 4670 m a.s.l.) in the ablation zone. Although at AWS1 site katabatic flow dominated most of the time, the bulk method was used to calculate the turbulent heat fluxes because wind speed maximum always remained above the measurement levels. The roughness length for momentum was calculated separately for ice and snow surfaces as 0.016 m and 0.001 m, respectively whereas roughness lengths for temperature and humidity were derived from the Reynolds number and the roughness length for momentum. Net short wave radiation was highly variable with lowest mean value (29 W m^{-2}) in winter to highest (202 W m^{-2}) in summer-monsoon period while net long wave radiation exerted lower seasonality with minimum values in post-monsoon and winter periods (−57 and −49 W m^{-2}, respectively) and maximum in summer-monsoon period (−13 W m^{-2}). In summer-monsoon period the melting conditions with high T_{surf} (mean = −0.1 °C) coincides with warm and humid conditions, associated with intense cloud covers, leading to high values of LWI and thus high net long wave radiation is observed. Net all-wave radiation was negative in post-monsoon and winter periods, indicative of radiative cooling of the glacier surface, whereas in summer-monsoon, it was the main heat source for melting. All the time, the atmosphere transported heat towards the glacier surface in the form of sensible heat flux. An interesting feature was observed in latent heat flux evolution that was continuously negative in post-monsoon and winter periods, thus sublimation predominated, while in summer-monsoon period, it switched to positive values indicating condensation or re-sublimation at the glacier surface. As a result of the SEB equation, energy was available for melting in summer-monsoon period only.

TCD
8, 2867–2922, 2014

Net all-wave radiation was the main heat flux towards surface with 82 % contribution while *H* and LE shared 13 % and 5 % of total heat flux, respectively.

This study highlights the impact of summer-monsoon snowfalls on glacier mass balance. Snowfall events during summer-monsoon season play an important role on melting via surface albedo. The intensity of these snowfalls during ablation period abruptly changes the surface conditions from ice to snow, hence melting is slowed down. Therefore, these snowfall events are among the most important drivers controlling the annual mass balance of Chhota Shigri Glacier. Summer-monsoon air temperature, controlling the precipitation phase (rain vs. snow and thus albedo), counts, indirectly, also among the most important drivers for the glacier mass balance.

A comparison of the SEB measured at the ablation zone of Chhota Shigri Glacier with those of other glaciers in High Asia Mountain shows that net short wave radiation flux is the largest energy and mainly controls the melt energy to the glacier surface whereas net long wave radiation flux is the greatest energy loss. In High Asia Mountain, sublimation predominates in summer-monsoon season over the ablation zone of the glaciers less affected by the ISM and submitted to drier conditions than those directly affected like Chhota Shigri Glacier, where LE brings a significant amount of energy at the glacier surface, in the form of condensation/re-sublimation.

The good validation of present model indicates that the model is reliable enough to make robust calculations of surface energy balance. In the upcoming future, this study would be useful to calibrate spatially distributed energy- and mass-balance models at glacier as well as regional scale. These models can be used to predict the future of water supply using different climate change projections.

Acknowledgements. This work has been supported by IRD as a part of M F Azam's PhD. Authors are also grateful to DST-IFCPAR/CEFIPRA project no. 3900-W1, the French Service d'Observation GLACIOCLIM as well as the Department of Science and Technology (DST), Government of India. We thank Indian meteorological Department (IMD), New Delhi India to provide the data from Bhuntar meteorological station. Authors thank Jawaharlal Nehru University, New Delhi for providing all the facilities to carry out this work. M F Azam is grateful to

TCD
8, 2867–2922, 2014

Rajdeep Singh for improving the content of the manuscript and R. Biron for sharing his knowledge and experience about AWS assembling.

References

Ageta, Y. and Higuchi, K.: Estimation of mass balance components of a summer-accumulation type glacier in the Nepal Himalaya, Geogr. Ann. A, 66, 249–255, 1984.

Aizen, V. B., Aizen, E. M., and Nikitin, S. A.: Glacier regime on the northern slope of the Himalaya (Xixibangma glaciers), Quatern. Int., 97–98, 27–39, doi:10.1016/S1040-6182(02)00049-6, 2002.

Andreas, E. L.: A theory for the scalar roughness and the scalar transfer coefficients over snow and sea ice, Bound.-Lay. Meteorol., 38, 159–184, 1987.

Arck, M. and Scherer, D.: Problems in the determination of sensible heat flux over snow, Geogr. Ann. A, 84, 157–169, 2002.

Azam, M. F., Wagnon, P., Ramanathan, AL., Vincent, C., Sharma, P., Arnaud, Y., Linda, A., Pottakkal, J. G., Chevallier, P., Singh, V. B., and Berthier, E.: From balance to imbalance: a shift in the dynamic behaviour of Chhota Shigri Glacier (Western Himalaya, India), J. Glaciol., 58, 315–324, doi:10.3189/2012JoG11J123, 2012.

Azam, M. F., Wagnon, P., Vincent, C., Ramanathan, AL., Linda, A., and Singh, V. B.: Reconstruction of the annual mass balance of Chhota Shigri Glacier (Western Himalaya, India) since 1969, Ann. Glaciol., 55, 69–80, doi:10.3189/2014AoG66A104, 2014.

Bahr, D. B., Dyurgerov, M., and Meier, M. F.: Sea-level rise from glaciers and ice caps: a lower bound, Geophys. Res. Lett., 36, L03501, doi:10.1029/2008GL036309, 2009.

Bintanja, R. and Van den Broeke, M. R.: The surface energy balance of Antarctic snow and blue ice, J. Appl. Meteorol., 34, 902–926, 1995.

Bookhagen, B. and Burbank, D. W.: Topography, relief, and TRMM-derived rainfall variations along the Himalaya, Geophys. Res. Lett., 33, L08405, doi:10.1029/2006GL026037, 2006.

Bookhagen, B. and Burbank, D. W.: Toward a complete Himalayan hydrological budget: spatiotemporal distribution of snowmelt and rainfall and their impact on river discharge, J. Geophys. Res., 115, F03019, doi:10.1029/2009JF001426, 2010.

TCD
8, 2867–2922, 2014

Bookhagen, B., Thiede, R. C., and Strecker, M. R.: Abnormal monsoon years and their control on erosion and sediment flux in high, arid northwest Himalaya, Earth Planet. Sci. Lett., 231, 131–146, 2005.
Bolch, T., Kulkarni, A., Kääb, A., Huggel, C., Paul, F., Cogley, J. G., Frey, H., Kargel, J. S., Fujita, K., Scheel, M., Bajracharya, S., and Stoffel, M.: The state and fate of Himalayan Glaciers, Science, 336, 310–314, 2012.
Brustaert, B.: Evaporation in the Atmosphere: Theory, History and Application, 299, Kluwer Acad., Norwell, Mass, 1982.
Cogley, J. G.: Present and future states of Himalaya and Karakoram glaciers, Ann. Glaciol., 52, 69–73, 2011.
Denby, B. and Greuell, W.: The use of bulk and profile methods for determining surface heat fluxes in the presence of glacier winds, J. Glaciol., 46, 445–452, 2000.
Favier, V., Wagnon, P., Chazarin, J. P., Maisincho, L., and Coudrain, A.: One-year measurements of surface heat budget on the ablation zone of Antizana Glacier 15, Ecuadorian Andes, J. Geophys. Res., 109, D18105, doi:10.1029/2003JD004359, 2004.
Favier, V., Agosta, C., Genthon, C., Arnaud, L., Trouvillez, A., and Gallée, H.: Modeling the mass and surface heat budgets in a coastal blue ice area of Adelie Land, Antarctica, J. Geophys. Res., 116, F03017, doi:10.1029/2010JF001939, 2011.
Gardelle, J., Berthier, E., Arnaud, Y., and Kääb, A.: Region-wide glacier mass balances over the Pamir-Karakoram-Himalaya during 1999–2011, The Cryosphere, 7, 1263–1286, doi:10.5194/tc-7-1263-2013, 2013.
Giesen, R. H., Andreassen, L. M., Van den Broeke, M. R., and Oerlemans, J.: Comparison of the meteorology and surface energy balance at Storbreen and Midtdalsbreen, two glaciers in southern Norway, The Cryosphere, 3, 57–74, doi:10.5194/tc-3-57-2009, 2009.
Giesen, R. H., Andreassen, L. M., Oerlemans, J., and Van den Broeke, M. R.: Surface energy balance in the ablation zone of Langfjordjøkelen, an arctic, maritime glacier in northern Norway, J. Glaciol., 60, 57–70, doi:10.3189/2014JoG13J063, 2014.
Greuell, W. and Smeets, P.: Variations with elevation in the surface energy balance on the Pasterze (Austria), J. Geophys. Res., 106, 31717–31727, 2001.
Greuell, W., Knap, W. H., and Smeets, P. C.: Elevational changes in meteorological variables along a mid-latitude glacier during summer, J. Geophys. Res., 102, 25941–25954, 1997.
Grisogono, B. and Oerlemans, J.: Justifying the WKB approximation in pure katabatic flows, Tellus A, 54, 453–463, 2002.

TCD
8, 2867–2922, 2014

Heid, T. and Kääb, A.: Repeat optical satellite images reveal widespread and long term decrease in land-terminating glacier speeds, The Cryosphere, 6, 467–478, doi:10.5194/tc-6-467-2012, 2012.
Hock, R. and Holmgren, B.: Some aspects of energy balance and ablation of Storglaciaren, Northern Sweden, Geogr. Ann. A, 78, 121–131, 1996.
Hoinkes, H. C.: Measurements of ablation and heat balance on alpine glacier, J. Glaciol., 2, 497–501, 1953.
Immerzeel, W. W., Pellicciotti, F., and Bierkens, M. F. P.: Rising river flows throughout the twenty-first century in two Himalayan glacierized watersheds, Nat. Geosci., 6, 742–745, 2013.
IPCC: Climate Change 2007: The Physical Science Basis. Contribution of Working Group I to the Fourth Assessment Report of the Intergovernmental Panel on Climate Change, edited by: Solomon, S., Qin, D., Manning, M., Chen, Z., Marquis, M., Averyt, K. B., Tignor, M., and Miller, H. L., Cambridge University Press, Cambridge, United Kingdom and New York, NY, USA, 2007.
IPCC: Climate Change 2013: The Physical Science Basis. Contribution of Working Group I to the Fifth Assessment Report of the Intergovernmental Panel on Climate Change, edited by: Stocker, T. F., Qin, D., Plattner, G.-K., Tignor, M., Allen, S. K., Boschung, J., Nauels, A., Xia, Y., Bex, V., and Midgley, P. M., Cambridge University Press, Cambridge, United Kingdom and New York, NY, USA, in press, 2013.
Iqbal, M.: An Introduction to Solar Radiation, Academic Press, New York, 1983.
Kääb, A., Berthier, E., Nuth, C., Gardelle, J., and Arnaud, Y.: Contrasting patterns of early 21st century glacier mass change in the Himalaya, Nature, 488, 495–498, doi:10.1038/nature11324, 2012.
Kaser, G., Großhauser, M., and Marzeion, B.: Contribution potential of glaciers to water availability in different climate regimes, P. Natl. Acad. Sci. USA, 107, 20223–20227, doi:10.1073/pnas.1008162107, 2010.
Kayastha, R. B., Ohata, T., and Ageta, Y.: Application of mass balance model to a Himalayan glacier, J. Glaciol., 45, 559–567, 1999.
Klok, E. J. L. and Oerlemans, J.: Model study of the spatial distribution of the energy and mass balance of Morteratschgletscher, Switzerland, J. Glaciol., 48, 505–518, 2002.
Klok, E. J., Nolan, M., and Van den Broeke, M. R.: Analysis of meteorological data and the surface energy balance of McCall Glacier, Alaska, USA, J. Glaciol., 51, 451–461, 2005.

TCD
8, 2867–2922, 2014

Koul, M. N. and Ganjoo, R. K.: Impact of inter- and intra-annual variation in weather parameters on mass balance and equilibrium line altitude of Naradu Glacier (Himachal Pradesh), NW Himalaya, India, Clim. Change, 99, 119–139, doi:10.1007/s10584-009-9660-9, 2010.

Kuipers Munneke, P., Van den Broeke, M. R., King, J. C., Gray, T., and Reijmer, C. H.: Near-surface climate and surface energy budget of Larsen C ice shelf, Antarctic Peninsula, The Cryosphere, 6, 353–363, doi:10.5194/tc-6-353-2012, 2012.

Lejeune, Y., Bertrand, J.-M., Wagnon, P., and Morin, S.: A physically based model of the year-round surface energy and mass balance of debris-covered glaciers, J. Glaciol., 59, 327–344, doi:10.3189/2013JoG12J149, 2013.

Li, J., Liu, S., Zhang, Y., and Shangguan, D.: Surface energy balance of Keqicar Glacier, Tianshan Mountains, China, during ablation period, Sciences in Cold and Arid Regions, 3, 197–205, doi:10.3724/SP.J.1226.2011.00197, 2011.

Marks, D. and Dozier, J.: Climate and energy exchange at the snow surface in the alpine region of the Sierra Nevada, 2, Snow cover energy balance, Water Resour. Res., 28, 3043–3054, 1992.

Maussion, F., Wei, Y., Huintjes, E., Pieczonka, T., Scherer, D., Yao, T., Kang, S., Bolch, T., Buchroithner, M., and Schneider, C.: Glaciological field studies at Zhadang Glacier (5500–6095 m), Tibetan Plateau, in: Workshop on the use of automatic measuring systems on glaciers – extended abstracts and recommendations of the IASC Workshop, edited by: Tijm-Reijmer, C. H., and Oerlemans, J., 23–26 March 2011, Pontresina (Switzerland), 62–68, Institute for Marine and Atmospheric Research, Utrecht University, 2011.

Meesters, A. G. C. A., Bink, N. J. H., Vugts, F., Cannemeijer, F., and Henneken, E. A. C.: Turbulence observations above a smooth melting surface on the Greenland Ice Sheet, Bound.-Lay. Meteorol., 85, 81–110, 1997.

Moore, R.: On the use of bulk aerodynamic formulae over melting snow, Nord. Hydrol., 14, 193–206, 1983.

Mölg, T. and Hardy, D. R.: Ablation and associated energy balance of a horizontal glacier surface on Kilimanjaro, J. Geophys. Res., 109, 1–13, doi:10.1029/2003JD004338, 2004.

Mölg, T., Cullen, N. J., and Kaser, G.: Solar radiation, cloudiness and longwave radiation over low-latitude glaciers: implications for mass-balance modelling, J. Glaciol., 55, 292–302, doi:10.3189/002214309788608822, 2009.

TCD
8, 2867–2922, 2014

Mölg, T., Maussion, F., Yang, W., and Scherer, D.: The footprint of Asian monsoon dynamics in the mass and energy balance of a Tibetan glacier, The Cryosphere, 6, 1445–1461, doi:10.5194/tc-6-1445-2012, 2012.
Nicholson, L. I., Prinz, R., Mölg, T., and Kaser, G.: Micrometeorological conditions and surface mass and energy fluxes on Lewis Glacier, Mt Kenya, in relation to other tropical glaciers, The Cryosphere, 7, 1205–1225, doi:10.5194/tc-7-1205-2013, 2013.
Oerlemans, J.: Analysis of a 3 year meteorological record from the ablation zone of Morteratschgletscher, Switzerland: energy and mass balance, J. Glaciol., 46, 571–579, 2000.
Oerlemans, J.: Glaciers and Climate Change, A. A. Balkema, the Netherlands, 2001.
Oerlemans, J.: The Microclimate of Valley Glaciers, Igitur, Utrecht University, 138 pp., ISBN 987-90-393-5303-5, Utrecht Publishing & Archiving Services, the Netherlands, 2010.
Oerlemans, J. and Klok, E.: Energy balance of a glacier surface: analysis of automatic weather station data from Morteratschgletscher, Switzerland, Arct. Antarct. Alp. Res., 34, 477–485, 2002.
Oke, T. R.: Boundary Layer Climates, 2nd edn., Routledge, 423 pp., 1987.
Ramanathan, AL.: Status Report on Chhota Shigri Glacier (Himachal Pradesh), Himalayan Glaciology Technical Report No. 1, Department of Science and Technology, Ministry of Science and Technology, New Delhi, 88 pp., 2011.
Reijmer, C. H. and Oerlemans, J.: Temporal and spatial variability of the surface energy balance in Dronning Maud Land, East Antarctica, J. Geophys. Res., 107, 4759–4770, doi:10.1029/2000JD000110, 2002.
Shekhar, M., Chand, H., Kumar, S., Srinivasan, K., and Ganju, A.: Climate-change studies in the western Himalaya, Ann. Glaciol., 51, 105–112, doi:10.3189/172756410791386508, 2010.
Sicart, J. E., Wagnon, P., and Ribstein, P.: Atmospheric controls of the heat balance of Zongo Glacier (16° S, Bolivia), J. Geophys. Res., 110, D12106, doi:10.1029/2004JD005732, 2005.
Sicart, J. E., Hock, R., Ribstein, P., Litt, M., and Ramirez, E.: Analysis of seasonal variations in mass balance and meltwater discharge of the tropical Zongo Glacier by application of a distributed energy balance model, J. Geophys. Res., 116, D13105, doi:10.1029/2010JD015105, 2011.
Smeets, C. J. P. P. and Van den Broeke, M. R.: The parameterisation of scalar transfer over rough ice surfaces, Bound.-Lay. Meteorol., 128, 339–355, 2008.
Sun, W., Qin, X., Du, W., Liu, W., Liu, Y., Zhang, T., Xu, Y., Zhao, Q., Wu, J., and Ren, J.: Ablation modeling and surface energy budget in the ablation zone of Laohugou glacier No. 12,

TCD
8, 2867–2922, 2014

western Qilian mountains, China, Ann. Glaciol., 55, 111–120, doi:10.3189/2014AoG66A902, 2014.
Thayyen, R. J. and Gergan, J. T.: Role of glaciers in watershed hydrology: a preliminary study of a "Himalayan catchment", The Cryosphere, 4, 115–128, doi:10.5194/tc-4-115-2010, 2010.
Thibert, E., Blanc, R., Vincent, C., and Eckert, N.: Glaciological and volumetric mass balance measurements: error analysis over 51 years for Glacier de Sarennes, French Alps, J. Glaciol., 54, 522–532, 2008.
Van den Broeke, M. R.: Momentum, heat and moisture budgets of the katabatic wind layer over a mid-latitude glacier in summer, J. Appl. Meteorol., 36, 763–774, 1997.
Van den Broeke, M. R., Van As, D., Reijmer, C. H., and Van de Wal, R. S. W.: Assessing and improving the quality of unattended radiation observations in Antarctica, J. Atmos. Ocean. Tech., 21, 1417–1431, 2004.
Van den Broeke, M. R., Smeets, C. J. P. P., and Van de Wal, R. S. W.: The seasonal cycle and interannual variability of surface energy balance and melt in the ablation zone of the west Greenland ice sheet, The Cryosphere, 5, 377–390, doi:10.5194/tc-5-377-2011, 2011.
Vincent, C., Ramanathan, Al., Wagnon, P., Dobhal, D. P., Linda, A., Berthier, E., Sharma, P., Arnaud, Y., Azam, M. F., Jose, P. G., and Gardelle, J.: Balanced conditions or slight mass gain of glaciers in the Lahaul and Spiti region (northern India, Himalaya) during the nineties preceded recent mass loss, The Cryosphere, 7, 569–582, doi:10.5194/tc-7-569-2013, 2013.
Wagnon, P., Ribstein, P., Francou, B., and Pouyaud, B.: Annual cycle of energy balance of Zongo Glacier, Cordillera Real, Bolivia, J. Geophys. Res., 104, 3907–3923, 1999.
Wagnon, P., Ribstein, P., Francou, B., and Sicart, J. E.: Anomalous heat and mass balance budget of Glaciar Zongo, Bolivia, during the 1997/98, El Nino year, J. Glaciol., 47, 21–28, 2001.
Wagnon, P., Sicart, J.-E., Berthier, E., and Chazarin, J.-P.: Wintertime high-altitude surface energy balance of a Bolivian glacier, Illimani, 6340 m above sea level, J. Geophys. Res., 108, 4177, doi:10.1029/2002JD002088, 2003.
Wagnon, P., Linda, A., Arnaud, Y., Kumar, R., Sharma, P., Vincent, C., Pottakkal, J. G., Berthier, E., Ramanathan, A., Hasnain, S. I., and Chevallier, P.: Four years of mass balance on Chhota Shigri Glacier, Himachal Pradesh, India, a new benchmark glacier in the western Himalaya, J. Glaciol., 53, 603–611, 2007.
Wagnon, P., Lafaysse, M., Lejeune, Y., Maisincho, L., Rojas, M., and Chazarin, J. P.: Understanding and modeling the physical processes that govern the melting of snow

TCD
8, 2867–2922, 2014

cover in a tropical mountain environment in Ecuador, J. Geophys. Res., 114, D19113, doi:10.1029/2009JD012292, 2009.
Wagnon, P., Vincent, C., Arnaud, Y., Berthier, E., Vuillermoz, E., Gruber, S., Ménégoz, M., Gilbert, A., Dumont, M., Shea, J. M., Stumm, D., and Pokhrel, B. K.: Seasonal and annual mass balances of Mera and Pokalde glaciers (Nepal Himalaya) since 2007, The Cryosphere, 7, 1769–1786, doi:10.5194/tc-7-1769-2013, 2013.
Weiers, S.: Zur Klimatologie des NW-Karakoram und angrenzender Gebiete. Statistische Analysen unter Einbeziehung von Wettersatellitenbildern und eines Geographischen Information systems (GIS), Bonner Geographische Abhandlungen, 92, Geographisches Institut, Universitat Bonn, Bonn, Germany, 1995.
Wulf, H., Bookhagen, B., and Scherler, D.: Seasonal precipitation gradients and their impact on fluvial sediment flux in the Northwest Himalaya, Geomorphology, 118, 13–21, 2010.
Yang, W., Guo, X., Yao, T., Yang, K., Zhao, L., Li, S., and Zhu, M.: Summertime surface energy budget and ablation modeling in the ablation zone of a maritime Tibetan glacier, J. Geophys. Res., 116, D14116, doi:10.1029/2010JD015183, 2011.
Zhang, G., Kang, S., Fujita, K., Huintjes, E., Xu, J., Yamazaki, T., Haginoya, S., Wei, Y., Scherer, D., Schneider, C., Yao, T.: Energy and mass balance of the Zhadang Glacier surface, central Tibetan Plateau, J. Glaciol., 213, 137–148, doi:10.3189/2013JoG12J152, 2013.

TCD
8, 2867–2922, 2014

Table 1. Measurement specification for AWS1 located at 4670 m a.s.l. on the middle of the ablation zone of Chhota Shigri Glacier, AWS2 located on a moraine at 4863 m a.s.l., and precipitation gauge installed at base camp (3850 m a.s.l.). Accumulation/Ablation at AWS1 was measured by SR50A sensor (Sect. 2.3). Variable symbols are also given. Sensor heights indicate the initial distances to the surface (12 August 2012).

Variable	symbol (unit)	Sensor	initial height (m)	stated accuracy
AWS1				
air temperature	T_{air} (°C)	Campbell HMP155A[a]	0.8 & 2.5	±0.1 at 0 °C
relative humidity	RH (%)	Campbell HMP155A[a]	0.8 & 2.5	±1 % RH at 15 °C
wind speed	u (m s^{-1})	A100LK, Vector Inst.	0.8 & 2.5	±0.1 m s^{-1} up to 10 m s^{-1}
wind direction	WD (degree)	W200P, Vector Inst.	2.5	±2 deg
incoming and outgoing short wave radiations	SWI, SWO (W m^{-2})	Kipp & Zonen CNR-4	1.8	±10 % day total
incoming and outgoing long wave radiations	LWI, LWO (W m^{-2})	Kipp & Zonen CNR-4	1.8	±10 % day total
air pressure	P_{air} (hPa)	Young 61302V	1	±0.3 hPa
accumulation/ablation	SR50A (m)	Campbell SR50A[b]	1.6[c]	±0.01 m or 0.4 % to target
AWS2				
air temperature	T_{air} (°C)	Campbell H3-S3-XT	1.5	±0.1 at 0 °C
relative humidity	RH (%)	Campbell H3-S3-XT	1.5	±1.5 % RH at 23 °C
wind speed	u (m s^{-1})	Campbell 05103-10-L	3.0	±0.3 m s^{-1}
incoming short wave radiation	SWI (W m^{-2})	Kipp & Zonen CNR-1	2.5	±10 % day total
incoming long wave radiation	LWI (W m^{-2})	Kipp & Zonen CNR-1	2.5	±10 % day total
Precipitation (base camp)	(mm)	Geonor T-200B	1.7 (inlet height)	±0.6 mm

[a] aspirated during daytime with RM Young 43502 radiation shields,
[b] mounted on a separated aluminum pole drilled into the ice,
[c] 1.6 m was initial height for SR50A sensor.

TCD
8, 2867–2922, 2014

Table 2. Seasonal means and annual mean (standard deviations) of T_{air}, RH, u and SWI over four hydrological years between 1 October 2009 and 30 September 2013 except for LWI (only three years between 1 October 2010 and 30 September 2013) at AWS2 (4863 m a.s.l.). P is the seasonal precipitation for one hydrological year between 1 October 2012 and 30 September 2013 at glacier base camp collected by the Geonor T-200B.

	Winter (DJFM)	Pre-monsoon (AM)	Summer-monsoon (JJAS)	Post-monsoon (ON)	Annual mean
T_{air} (°C)	−13.4 (0.9)	−5.3 (0.7)	2.5 (0.6)	−7.8 (1.4)	−5.8 (0.2)
RH (%)	42 (2)	52 (2)	68 (1)	39 (6)	52 (2)
u (m s^{-1})	5.5 (0.6)	3.5 (0.2)	2.8 (0.1)	4.4 (0.5)	4.1 (0.2)
SWI (W m^{-2})	161 (12)	299 (34)	266 (7)	176 (18)	221 (14)
LWI (W m^{-2})	192 (3)	231 (2)	289 (17)	187 (8)	230 (6)
P (mm w.e.)	679	148	117	32	976

TCD
8, 2867–2922, 2014

Table 3. 60 day means (standard deviations) of meteorological and SEB variables measured or computed at AWS1 (4670 m a.s.l.) on Chhota Shigri Glacier for different representative periods. The symbols for variables are described in the text. SWN, LWN, and R are net short-wave, long-wave and all-wave radiations, respectively.

Variable	Post-monsoon (1 Oct 2012–29 Nov 2012)	Winter (1 Dec 2012–29 Jan 2013)	Summer-monsoon (8 Jul 2013–5 Sep 2013)
T_{air} (°C)	−8.6 (2.5)	−14.8 (3.7)	3.6 (1.2)
RH (%)	49 (12)	44 (17)	82 (5)
u (m s^{-1})	4.7 (0.7)	4.9 (1.1)	3.6 (0.5)
STOA (W m^{-2})	276 (39)	216 (11)	458 (25)
SWI (W m^{-2})	175 (46)	130 (44)	248 (67)
SWO (W m^{-2})	127 (31)	101 (32)	47 (15)
α_{acc}	0.73 (0.04)	0.79 (0.04)	0.19 (0.02)
Cloud factor	0.28 (0.26)	0.29 (0.33)	0.36 (0.24)
LWI (W m^{-2})	205 (23)	189 (36)	300 (20)
LWO (W m^{-2})	262 (11)	238 (16)	314 (1)
T_{surf} (°C)	−12.7 (2.8)	−18.9 (4.5)	−0.1 (0.3)
SWN (W m^{-2})	48 (17)	29 (13)	202 (53)
LWN (W m^{-2})	−57 (19)	−49 (22)	−13 (19)
R (W m^{-2})	−9 (18)	−20 (13)	188 (45)
H (W m^{-2})	30 (11)	33 (16)	31 (10)
LE (W m^{-2})	−25 (9)	−20 (9)	11 (13)
H + LE (W m^{-2})	5 (12)	13 (16)	42 (21)
Q (W m^{-2})	−4 (16)	−7 (9)	230 (60)
Precipitation (mm w.e. d^{-1})	0.6 (1.0)	5.0 (8.9)	0.5 (0.9)
Snow (mm w.e. d^{-1})	5.3 (5.1)	6.3 (13.0)	1.4 (1.6)
Melting (mm w.e. d^{-1})	0.7 (1.9)	0.0 (0.0)	60.9 (15.1)
Subl. (–)/Cond. (+) (mm w.e. d^{-1})*	−0.8 (0.3)	−0.6 (0.3)	0.3 (0.4)

* negative for sublimation, positive for condensation or re-sublimation.

TCD
8, 2867–2922, 2014

Table 4. Comparison of SEB components on different glaciers in High Asia Mountain glaciers. All fluxes are in $W\,m^{-2}$, Values in brackets are the % contribution of each energy flux.

Glacier	Altitude (m a.s.l.)	Region (ISM dominated, Y or N)	Period of observation	R ($W\,m^{-2}$)	H ($W\,m^{-2}$)	LE ($W\,m^{-2}$)	Rest ($W\,m^{-2}$)	Q ($W\,m^{-2}$)	Reference
Glacier AX010	4960	central Himalaya, Nepal (Y)	25 May–25 Sep 1978	64 (85)	8 (10)	4 (5)	n/a	74 (100)	Kayastha et al. (1999)
Glacier AX010	5080	central Himalaya, Nepal (Y)	25 May–25 Sep 1978	55 (83)	8 (12)	3 (5)	n/a	63 (100)	Kayastha et al. (1999)
Xixibangma	5700	south central TP[a] (N)	23 Aug–11 Sep 1991	28 (86)	5 (14)	−19 (57)	n/a	14(43)	Aizen et al. (2002)
Parlung No. 4	4800	southeast TP (Y)	21 May–8 Sep 2009	150 (84)	28 (16)	−1 (1)	−1 (1)	176 (98)	Yang et al. (2011)
Zhadang	5660	central TP (N)	1 May–30 Sep 2010	62 (86)	10 (14)	−8 (11)	−4 (5)	−61 (84)	Zhang et al. (2013)
Zhadang	5660	central TP (N)	1 May–15 Sep 2011	27 (77)	8 (23)	−10 (28)	−2 (5)	−24 (67)	Zhang et al. (2013)
Keqicar	4265	southwest Tianshan (N)	16 Jun–7 Sep 2005[b]	63 (81)	14 (19)	−54 (70)	n/a	23 (30)	Li et al. (2011)
Laohugou No. 12	4550	western Qilian, China (N)	1 Jun–30 Sep 2011	81 (93)	7 (7)	−13 (15)	n/a	75 (85)	Sun et al. (2014)
Chhota Shigri	4670	western Himalaya, India (Y)	8 Jul–5 Sep 2013	188 (82)	31 (13)	11 (5)	n/a	230 (100)	Present study

[a] TP = Tibetan Plateau, [b] with a gap of 1 July to 7 August 2005.

TCD
8, 2867–2922, 2014

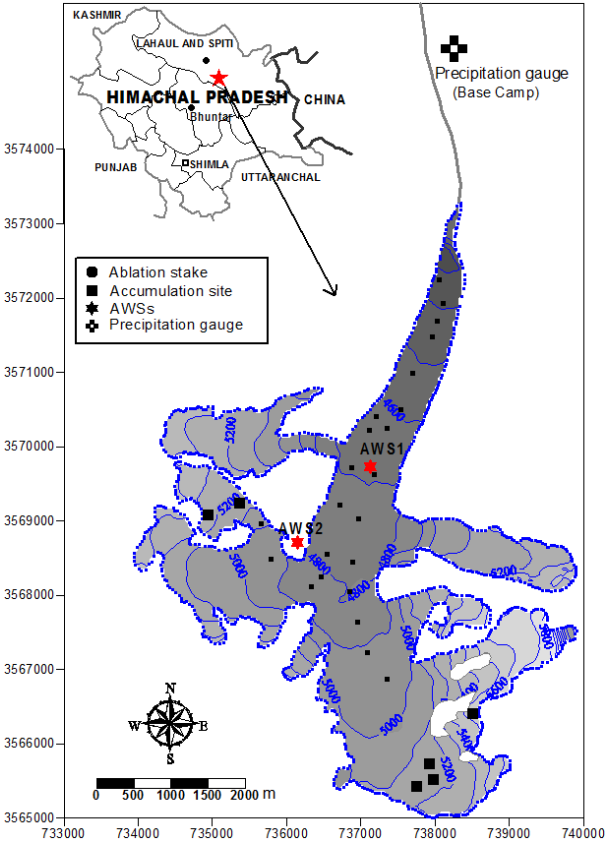

Figure 1. Map of Chhota Shigri Glacier showing the ablation stakes (black small squares), accumulation sites (black big squares), AWSs (red stars) and precipitation gauge (black cross). The map coordinates are in the UTM43 (north) World Geodetic System 1984 (WGS84) reference system.

TCD
8, 2867–2922, 2014

Figure 2. Photographs of AWS1 on Chhota Shigri Glacier taken on 09 October 2012 (left panel) and on 22 August 2013 (right panel) (©: Mohd. Farooq Azam). SR50A mounted on a separated pole drilled into the ice, is visible at the left of AWS1.

TCD
8, 2867–2922, 2014

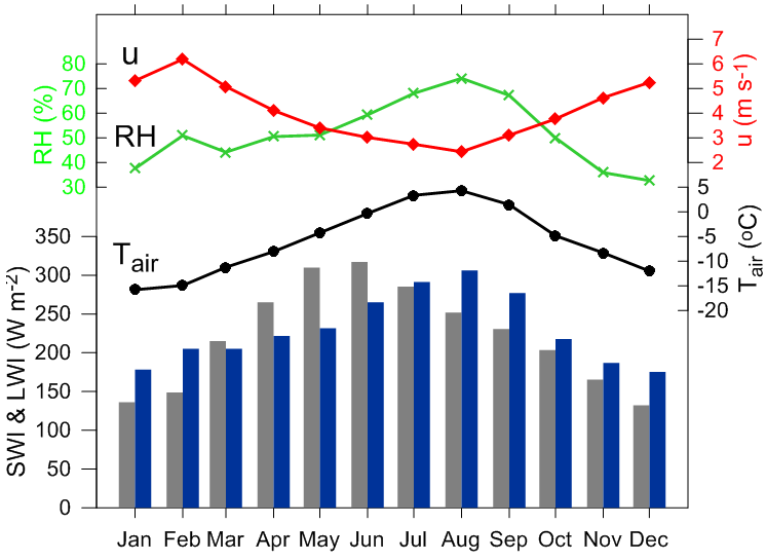

Figure 3. Mean monthly values of T_{air} (black dots), RH (green crosses), u (red squares), SWI (grey bars) and LWI (blue bars) at AWS2 (4863 m a.s.l.). T_{air}, RH, u and SWI are the mean monthly values of four hydrological years between 1 October 2009 and 30 September 2013 while LWI are the mean monthly values of three hydrological years between 1 October 2010 and 30 September 2013.

TCD
8, 2867–2922, 2014

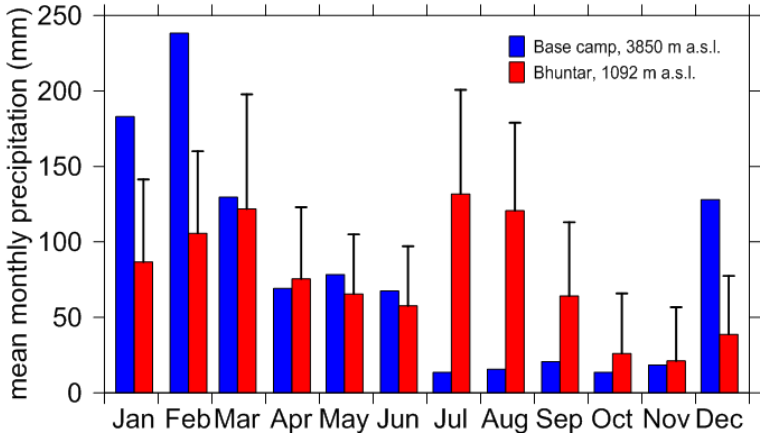

Figure 4. Comparison of monthly precipitations (blue bars) at Chhota Shigri base camp for 2012/2013 hydrological year with the mean monthly precipitations (red bars) between 1969 and 2013 at Bhuntar meteorological station. The error bars represent the standard deviation (1σ) of the monthly precipitation mean.

TCD
8, 2867–2922, 2014

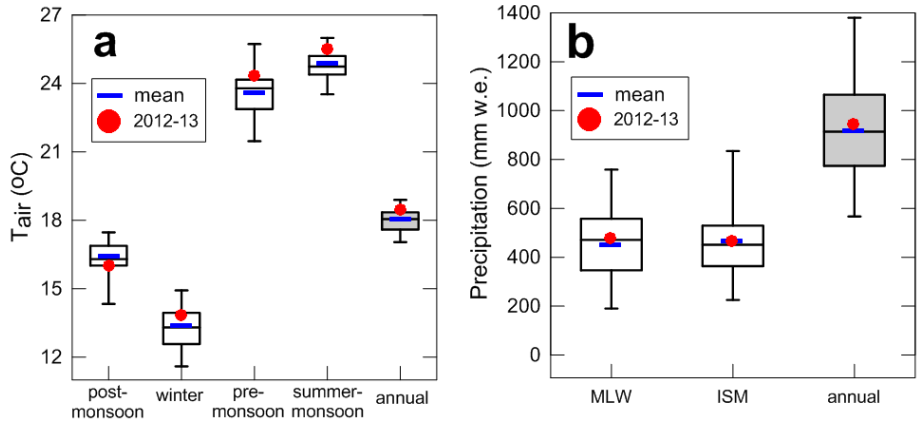

Figure 5. Boxplots of seasonal and annual T_{air} **(a)** and precipitation **(b)** obtained from 44 hydrological years (1969 to 2013) from Bhuntar meteorological station. Boxes cover the 25th to the 75th percentile of each distribution with a central line as the median. The blue thick horizontal line is the 1969–2013 mean, red dot is the 2012/2013 hydrological year mean.

TCD
8, 2867–2922, 2014

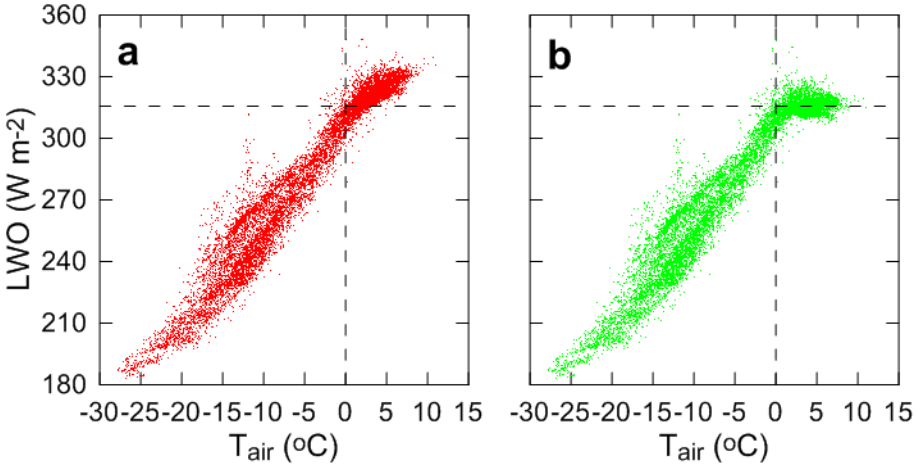

Figure 6. Half-hourly values of LWO as a function of T_{air}, **(a)** before and **(b)** after applying the correction for T_{air} above 0 °C. The dashed lines indicate 0 °C and 315.6 W m^{-2}, the maximum LWO for a melting surface.

TCD
8, 2867–2922, 2014

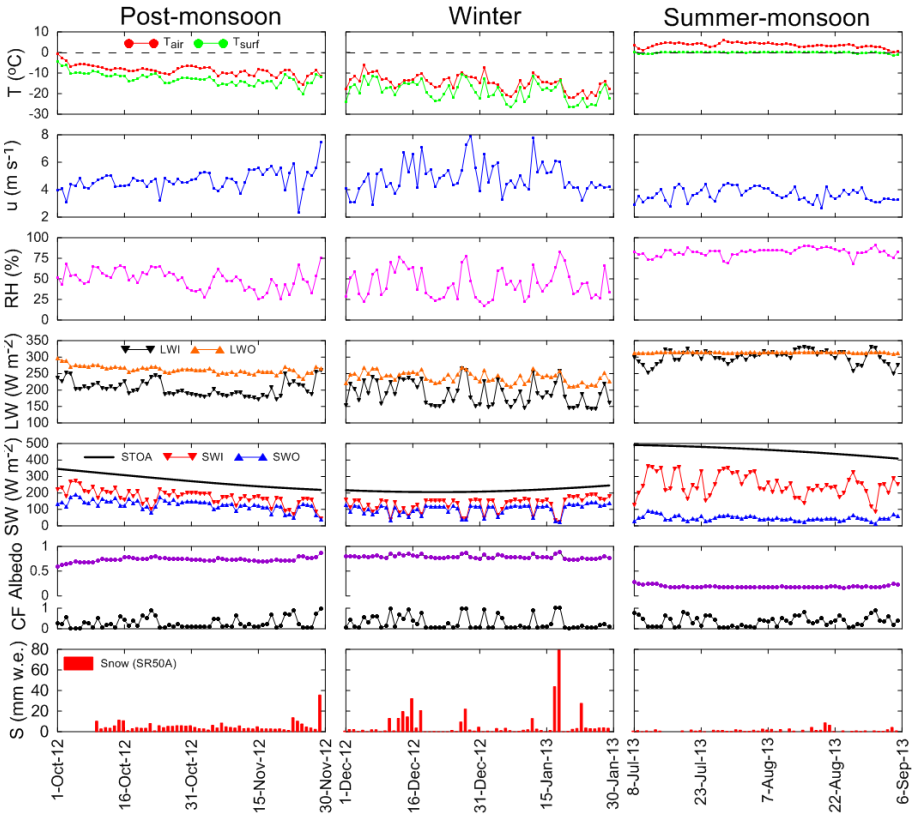

Figure 7. Daily meteorological variables recorded at AWS1 (4670 m a.s.l.) as representative of post-monsoon (1 October to 29 November 2012), winter (1 December to 29 January 2013) and summer-monsoon (8 July to 5 September 2013) periods. Also shown (lower panel) are the snow falls derived from SR50A data at AWS1.

TCD
8, 2867–2922, 2014

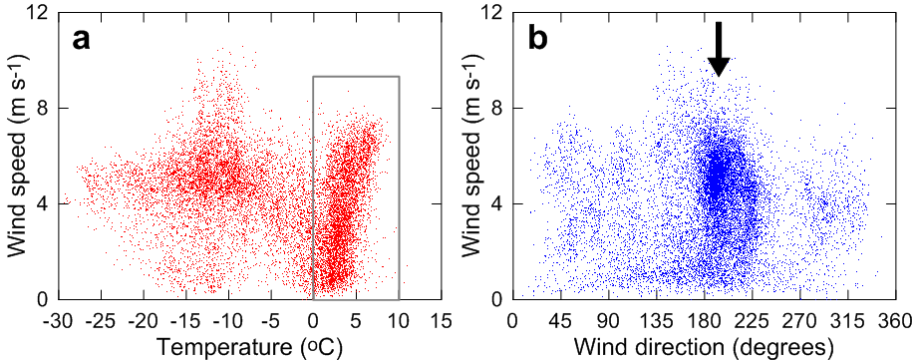

Figure 8. Scatter plots showing relations between u, T_{air} and WD. In both panels (**a** and **b**) all the available measurements are shown, and every dot represents a half-hourly mean value. The inset in **(a)** highlights the relationship between u and T_{air} above 0 °C. The arrow in **(b)** indicates the direction of the local flow line of the glacier.

TCD
8, 2867–2922, 2014

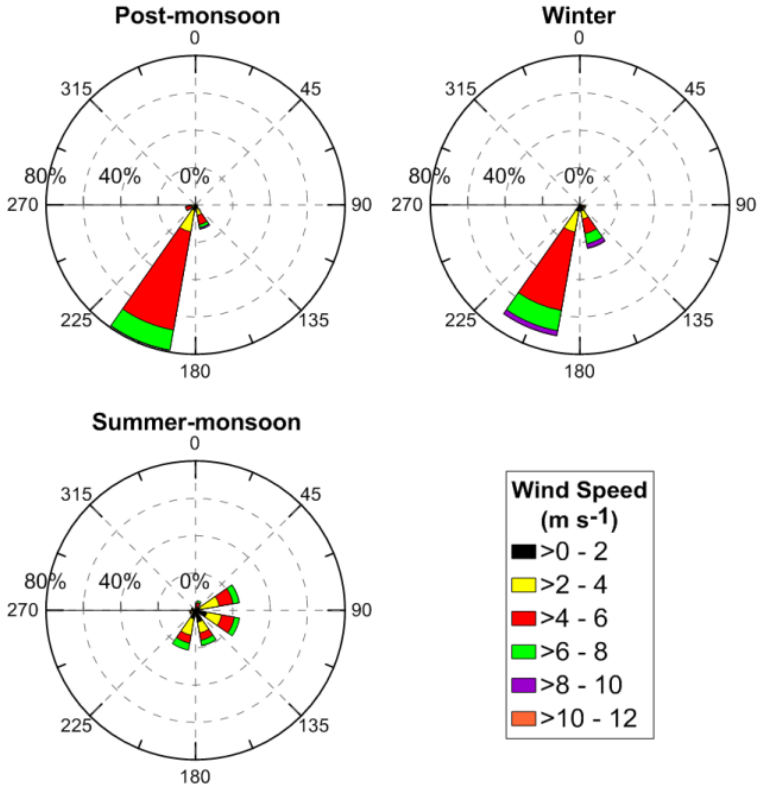

Figure 9. WD and *u* (half-hourly means) at AWS1 for post-monsoon, winter and summer-monsoon representative periods. The frequency of WD is expressed as percentage over the entire observational period (indicated on the radial axes).

TCD
8, 2867–2922, 2014

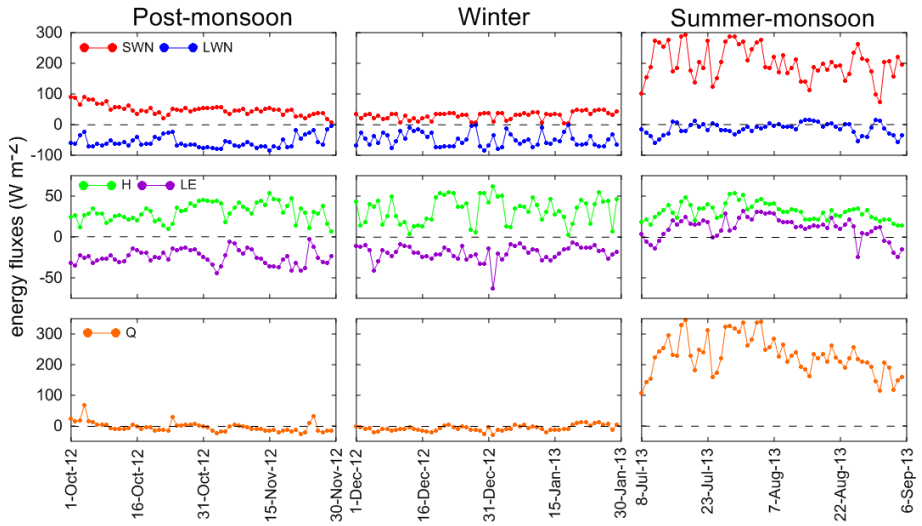

Figure 10. Daily values of the surface energy fluxes at AWS1 (4670 m a.s.l.) as representative of post-monsoon (1 October to 29 November 2012), winter (1 December to 29 January 2013) and summer-monsoon (8 July to 5 September 2013) periods. SWN, LWN and *Q* are the net short wave, net long wave radiations and net heat flux, respectively.

TCD
8, 2867–2922, 2014

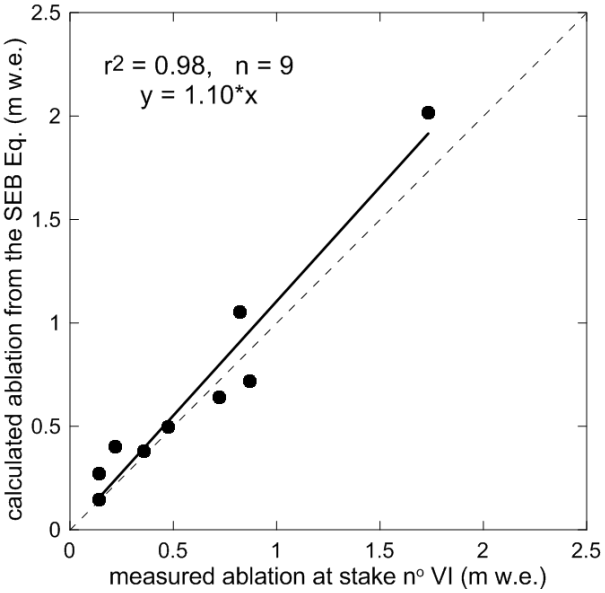

Figure 11. Comparison between ablation computed from the SEB Eq. and measured at stake no. VI during several few-day to few-week periods of 2012 and 2013 summers where field measurements are available. Also shown are the 1 : 1 line (dashed line) and the regression line (solid line).

TCD
8, 2867–2922, 2014

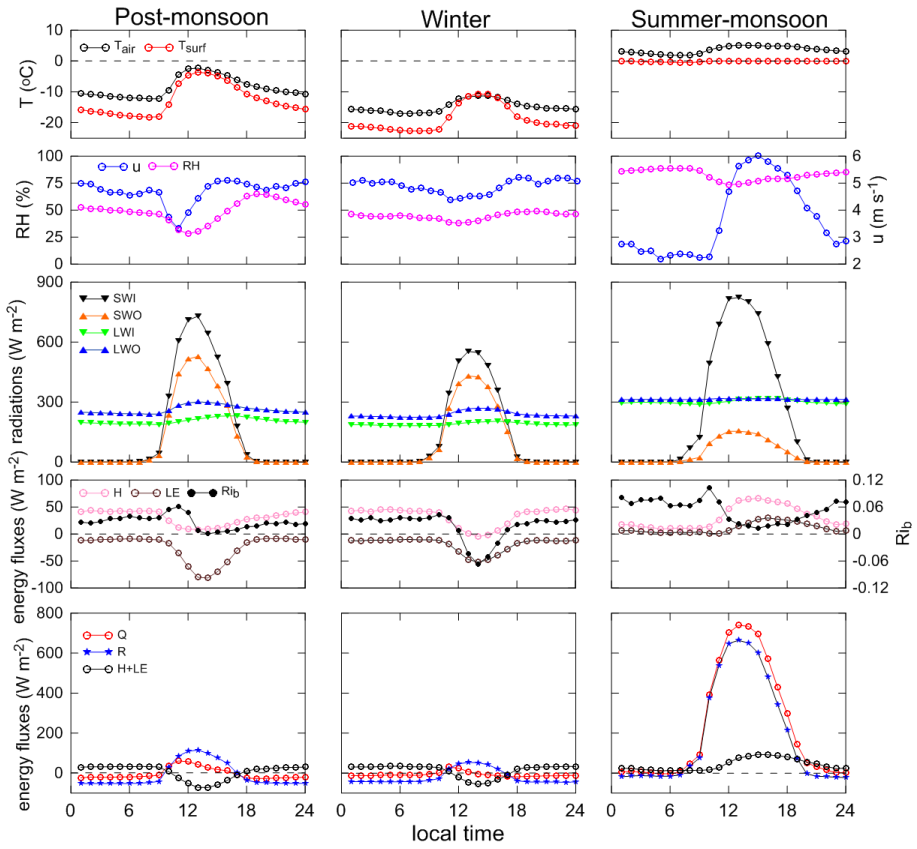

Figure 12. Mean diurnal cycle of meteorological and SEB variables at AWS1 (4670 m a.s.l.) as representative of post-monsoon (1 October to 29 November 2012), winter (1 December to 29 January 2013) and summer-monsoon (8 July to 5 September 2013) periods.

TCD
8, 2867–2922, 2014

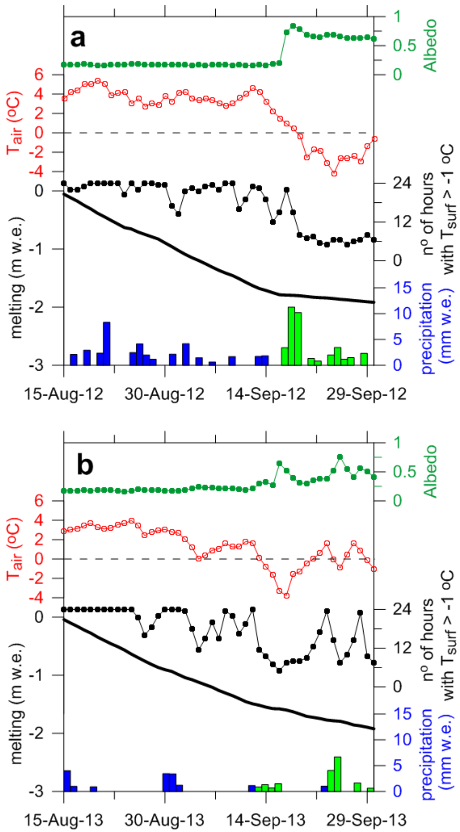

Figure 13. Comparison of computed cumulative melting (black thick line) between 15 August and 30 September from summers 2012 **(a)** and 2013 **(b)**. Also shown are the mean T_{air} (red open dots), the number of hours in a day when T_{surf} is $> -1\,^{\circ}$C (black dots), daily albedo (dark green dots) and the precipitations as rain/snow obtained from records at base camp (blue and green bars, respectively).

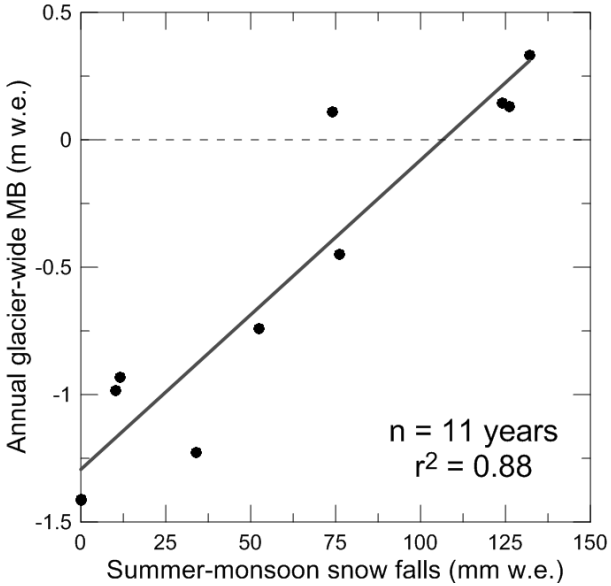

Figure 14. Annual glacier-wide mass balance as a function of the sum of the 3 largest summer-monsoon daily snowfalls assessed from precipitation record from Bhuntar meteorological station (see text for details) between 2002 and 2013.

TCD
8, 2867–2922, 2014